CHALMERS
UNIVERSITY OF TECHNOLOGY

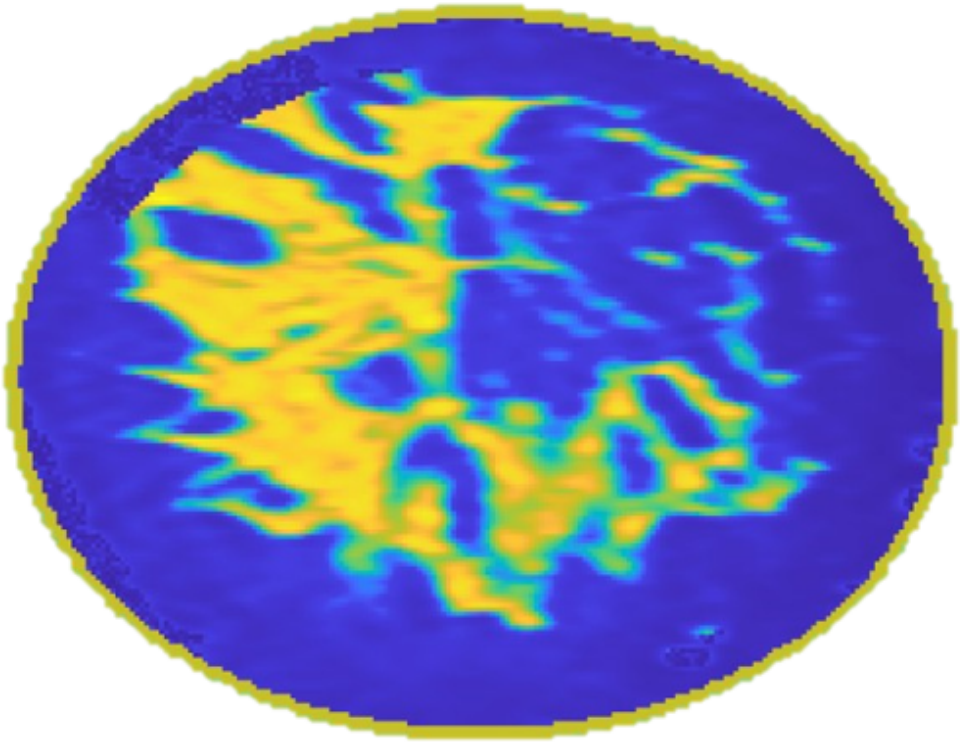

Reconstruction of Microwave Tomography for Breast Cancer Detection

Evaluation of a Discrete Dipole Approximation Method

Master's Thesis in Biomedical Engineering

EMELIE BJÖRKMAN

DEPARTMENT OF ELECTRICAL ENGINEERING
CHALMERS UNIVERSITY OF TECHNOLOGY
Gothenburg, Sweden 2023
www.chalmers.se

Master's thesis 2023

Reconstruction of Microwave Tomography for Breast Cancer Detection

Evaluation of a Discrete Dipole Approximation Method

EMELIE BJÖRKMAN

CHALMERS
UNIVERSITY OF TECHNOLOGY

Department of Electrical Engineering
Signal Processing and Biomedical Engineering
Biomedical Electromagnetics
Chalmers University of Technology
Gothenburg, Sweden 2023

Reconstruction of Microwave Tomography for Breast Cancer Detection
Evaluation of a Discrete Dipole Approximation Method
EMELIE BJÖRKMAN

Supervisor: Andreas Fhager, Department of Electrical Engineering
Examiner: Andreas Fhager, Department of Electrical Engineering

Master's Thesis 2023
Department of Electrical Engineering
Signal Processing and Biomedical Engineering
Biomedical Electromagnetics
Chalmers University of Technology
SE-412 96 Gothenburg
Telephone +46 31 772 1000

Cover: The dielectric distribution of the permittivity in a MRI phantom.

Typeset in LaTeX
Printed by Chalmers Reproservice
Gothenburg, Sweden 2023

To all women
Since women's health care should be harmless and painfree

Reconstruction of Microwave Tomography for Breast Cancer Detection
Evaluation of a Discrete Dipole Approximation Method
EMELIE BJÖRKMAN
Department of Electrical Engieering
Chalmers University of Technology

Abstract

Breast cancer is the most prevalent cancer worldwide, affecting mostly women but men as well. The survival rates have increased dramatically over the last 50 years, primarily due to early detection protocols and enhanced treatment options. However, today's screening techniques consisting mainly of x-ray mammography is both uncomfortable and contains harmful radiation. Depending on the breast type, it is also common with both false positives and fully omitted small tumours. Reconstruction using microwave tomography is a promising alternative, but is computationally heavy requiring tens of hours to reconstruct a single image and expensive hardware accurately collect the data. In this thesis, an approach using a discrete dipole approximation has been evaluated and compared to results from electromagnetic simulations in COMSOL Multiphysics as well as results from a finite-difference time-domain method. The suggested dipole method for reconstruction is a continuation of work conducted at Chalmers in collaboration with Dartmouth. The results are positive, indicating good detection for small objects, especially those with higher dielectric properties than the background material, which are exactly those objects omitted with traditional screening. The reconstruction of these objects are also good. However, for larger objects, especially those with lower dielectric properties than the background, and for more complex geometries, more evaluations needs to be performed.

Keywords: breast cancer, imaging techniques, microwave tomography, discrete dipole approximation, forward solution.

Acknowledgements

This thanks goes beyond the scope of this single report. My master thesis has been my dream project, a worthy ending to my time at Chalmers as a student. This goes out to all the friends I have made along the way for motivating me, making me laugh, helping me and for making me stick around till the end by generally surviving and overcoming the courses with me. I am thankful to the Physics Student Union Division and the Chalmers Student Union for all the personal development and love. The memories made through my many engagements will stay with my for life.

I want to send a big thank you to my supervisor Associate Professor Andreas Fhager. He agreed to this thesis adventure without hesitation, supported me throughout the project and never doubted nor questioned me. I also want to thank PhD Candidate Seyed Moein Pishnamaz for helping me with all my COMSOL questions, without him the results would not have been the same.

Finally, and most importantly, I want to thank my family for always supporting, trusting and helping me as well as believing I knew what I was doing.

Emelie Björkman, Gothenburg, June 2023

List of Acronyms

Below is the list of acronyms that have been used throughout this thesis listed in alphabetical order:

CT	Computerized Tomography
DDA	Discrete Dipole Approximation
FDTD	Finite-Difference Time-Domain
FEM	Finite Element Method
MRI	Magnetic Resonance Imaging
MT	Microwave Tomography
PET	Position Emission Tomography
RMS	Root Mean Square Error

List of Nomenclature

Below is the nomenclature of indices, parameters, sets and variables that have been used throughout this thesis.

General

$\bar{x}$	Notation for vector
$\bar{\bar{x}}$	Notation for matrix
i	Imaginary unit
ω	Frequency
τ	Dielectric relaxation time constant

Electromagnetics

$\bar{B}$	Magnetic flux density
$\bar{D}$	Displacement field
$\bar{E}$	Electric field
$\bar{E}_{inc}$	Incident electric field
$\bar{E}_{loc}$	Electric field sensed by each molecule, microscopic level
E_{scat}	Scattered electric field
$\bar{E}_{tot}$	Total electric field, macroscopic level
$\bar{H}$	Magnetic field
$\bar{J}$	Free current density
α	Exponent parameter
ϵ	Environment permittivity
ϵ_0	Free-space permittivity
ϵ_r	Relative permittivity
ϵ^*	Complex dielectric constant

ϵ_s	Static dielectric constant
ϵ_∞	Infinite frequency dielectric constant
k	Wavenumber
k_b	Background wavenumber
μ	Environment permeability
μ_0	Free-space permeability
μ_r	Relative permeability
σ	Electrical conductivity
ρ	Charge density

Algorithm

D	Image domain
D_i	Dipole cells
$\bar{\bar{G}}_{ij}$	Dipole interactions
$\bar{P}$	Polarization
$\bar{R}_i$	Distance to transmitting antenna
r_i,r_j	Dipole locations
$\bar{r}_{ij}$	Distance between two dipoles
α	Polarizability term
χ	Susceptibility
H_0^2	The Hankel function, zero-order, second kind
I_0	Amplitude of applied current
N	Number of molecules per unit volume
n	Number of dipoles

Contents

List of Figures

List of Tables

1
Introduction

Breast cancer is the most incident and prevalent cancer in the world, having recently surpassed lung cancer on the list [1, 2]. The disease affects both men and women, however, in 2020 alone 2.3 million people were diagnosed globally, out of which more than 99 % were women [3]. Breast cancer alone stands for 25 % of all cancer diagnoses for women and out of the 2.3 million diagnosed patients almost 700 000 died from the disease, that is over 30 % [1, 2]. The prevalence after five years is 7.7 million, meaning at least that many women are in this now living every day with breast cancer [1, 2]. The cancer arises in the fibroglandular tissue of the breast and what starts of as a non-symptomatic and non-threatening condition will with time, if left untreated, progress into a life threatening situation through the metastasising of the cancer to surrounding tissue and eventually even organs [1]. Our more Western life-style, with e.g. less exercise and increased alcohol consumption, could be a great cause behind the increased incidence and lowered average age of initial illness in recent years [4]. The incidence is higher in industrialized countries than it is in many countries in Asia and Africa [4]. It has also been seen in e.g China that the incidence has increased accordingly with the adaption of the Western living standard [4]. Considering the high incident for breast cancer, the mortality rate is however relatively low compared to other cancer types. This could be explained with the technical development and increased medical understanding, leading to regulated screening protocols and enhanced treatment options in the last 50 years [5]. Several reports have proved that the single most important factor for long-term survival is early detection [1, 4, 6]. If the disease is identified early, the chances of treatment being effective is highly increased [1]. A woman in Europe has on average an 11 % risk of developing breast cancer but in high-income countries, the survival rate five years after diagnosis is 90 %, while it's only 66 % in India and as low as 40 % in South Africa [1, 4]. This proves early detection and treatment is key and should be applied globally [1]. In high-income countries the annual breast cancer mortality has been reduced by 2-4 %, and if this were to be the case worldwide, the lives of around 2.5 million women could be saved in the next two decades [1].

Mammography is the most common screening method and is offered to all women over the age of 40 in most high-income countries [3]. However, though being the primary screening method it has well documented weaknesses when it comes to sensitivity and specificity [6]. Mammography is also considered uncomfortable and even painful [3]. It is time for an affordable, easy, pain free and harmless screening method. Microwave imaging is proving to be a promising alternative for breast cancer detection, using electromagnetic waves with frequencies around 500 MHz - 3 GHz [5, 6, 7]. The morphology of breast tissue seems ideal for microwave imaging

given that the dielectric properties, such as permittivity and conductivity, of adipose tissue are lower than that of fibroglandular tissue, which in turn are often lower then that of tumours [6]. Notwithstanding its performance the screening method still remains mainly academic, gaining little clinical acceptance [6]. The reasons for this are partly hardware and partly software related. It is hard to collect accurate data and it takes tens of hours to reconstruct a single image from said data [6].

In an ongoing collaborating project at Chalmers University of Technology and Dartmouth Collage, electromagnetic measurement systems are being developed for breast cancer detection using microwave tomography image reconstruction. Several different forward solution methods as well as reconstruction algorithms have been used with successful results. The technology works, however the computational load remains an obstacle. A PhD candidate, Samar Hosseinzadegan, at Chalmers in the Biomedical Electromagnetics group, developed a new fast 2D reconstruction algorithm for these electromagnetic measurement systems, based on a discrete dipole approximation method. This algorithm can reconstruct images in less than 3 minutes and have been proven to work good with only 20 iterations for objects with $r < 2$ cm and dielectric properties close to the background. However, the accuracy of the reconstruction algorithm needs to be tested on more input data, for larger sizes, more deviating dielectric properties as well as more complex geometries.

1.1 Aims

The aim of this thesis has been to validate and evaluate accuracy of the fast 2D discrete dipole approximation method as a numerical forward solution algorithm used to reconstruct images for breast cancer detection. In order to further explore the limitations in computational resources required to reconstruct images for breast cancer detection using Chalmers' and Dartmouth's microwave tomography measurement systems, input data has been simulated to explore the effect of an object's size, dielectric properties, as well as geometric complexity. Different forward solution methods have been applied to generate the input electromagnetic fields used in the reconstruction algorithm. These different forward solutions have also been compared to one another to establish the reliability of the discrete dipole approximation.

1.2 Scope

In this thesis only the accuracy of the 2D discrete dipole approximation with respect to size, dielectric properties and complexity of the objects have been investigated. The physical settings have been considered to be fixed, as has the dielectric properties of the background. The implementations of the forward solutions and reconstruction algorithm has not been altered with either, aside from the number of iterations.

2

Theory

In this chapter a description of the relevant parts of microwave tomography is given, including breast anatomy, biological electromagnetics and the reconstruction algorithm.

2.1 Breast Anatomy and Cancer Formation

The female human breast consists of two main types of tissue: adipose (fat) and fibroglandular (connective tissue and glands) [7]. The ratio between adipose and fibroglandular tissue in the breast varies a lot between individuals, from nearly 100 % adipose to nearly 100 % fibroglandular tissue [4]. Breasts can be medically categorized into four groups depending on their fibroglandular density: *fatty* (almost entirely fat), *scattered* (scattered regions of fibroglandular tissue), *heterogeneously dense* (mostly fibroglandular tissue) and *extremely dense* breasts (almost no fat), see Figure 2.1 [7, 8, 9].

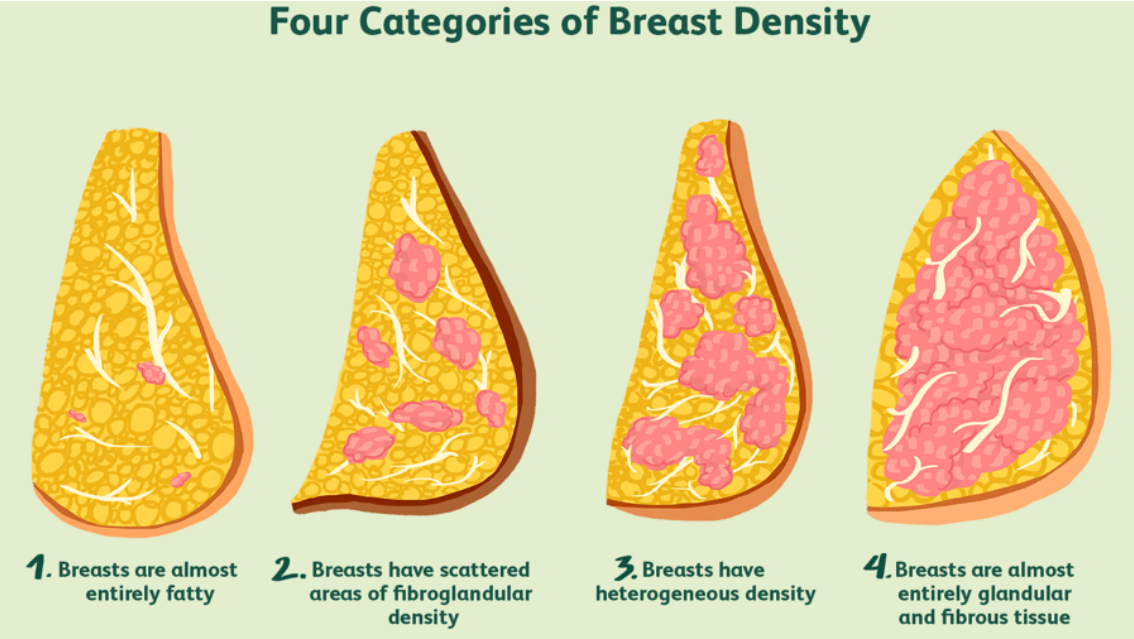

Figure 2.1: The formation and differences between the four breast types [10].

Breast cancer can occur with both men and women, but only around 0.8 % of all cases are men [2, 5]. Typically, cancer and tumours are the result of gene mutations

causing uncontrolled, irregular and chaotic cell growth and cell division [5]. Tumours can occur in both the adipose and fibroglandular breast tissue but primarily affect the glands including the lobules and ducts [5]. Depending on the growth pattern (invasive or non-invasive) and location (ductal or lobular) of the cancer, it can be categorized into four main kinds: *non-invasive ductal carcinoma, non-invasive lobular carcinoma, invasive ductal carcinoma and invasive lobular carcinoma*, where invasive ductal carcinoma is the most frequently occurring type.

2.2 Risk Factors

There are several risk factors for women developing breast cancer, including genetics, reproductive and hormonal changes, life style, demographic, environment and age to mention a few [4, 5]. Genetics, ageing and reproductive factors are simply facts of life, though it has been seen that women with a late onset of menarche or early onset of menopause have a decreased risk of developing breast cancer, as do women who bear children and especially those who breast feed their babies [4]. On the other hand, our increased Western living standards have been proved to increase the breast cancer risk; less exercise, obesity, alcohol consumption and even disturbed sleeping patterns and decreased production of melatonin due to artificial light have all proved to have negative effects on our health [4].

Breast cancer has been proven more common in dense breasts than in fatty ones, and the risk increases the denser the breast [9]. Those with dense breasts have a 4-6 times higher risk of getting breast cancer than those with a high adipose ratio [3]. Almost half of all mammograms performed on women over the age of 40 showed dense breast types (40 % dense, 10 % extremely dense) [3, 9]. The density is important in the detection of tumours [7]. Tumours, lesions and calcifications have apparent similarities to glands and pathological breast alterations, making them hard to identify in denser breast types using traditional mammography, since they all appear as white regions [7, 9]. The lack of adipose tissue and high ratio of fibroglandular tissue in heterogeneously dense breasts and extremely dense breasts lowers the sensitivity of mammography and small masses may be obscured [8].

2.3 Breast Cancer Screening Techniques

There are a number of methods to examine the breasts in search of cancer, monitor treatment progress and determine tumour development, including x-ray mammography, magnetic resonance imaging (MRI), computerized tomography (CT) and position emission tomography (PET) [5]. Additionally, new methods such as digital breast tomosynthesis, contrast mammography, and contrast-enhanced MRI can also be used in both screening and diagnosis [11].

2.3.1 X-ray Mammography

X-ray mammography is the primary routine screening method for detecting breast cancer and is recommended to all women between the ages of 40-74 in Sweden, 50-

74 in USA and 50-69 in Canada, since early detection has proven vital [3, 12, 13]. Mammography is performed using an x-ray machine in order to detect and treat breast cancer at an early stage, the operating principle being visualizing the grey-scale contrasts between different breast tissues [3, 5]. A camera photographs the inside of the breast while a plate is pressing down and squeezing the breast, creating 2D projections of the breast from two angles: craniocaudal (top-bottom view) and mediolateral oblique (side view) [3, 5]. In the case of detecting a suspicious mass, additional craniocaudal views or spot compression may be taken [5]. Firm and even compression is needed to ensure high contrast and good resolution, but it also causes the patient discomfort or even pain [5].

The advantages of mammography is that regular examination leads to early detection which reduces the risk of metastasis, increases the chance of full recovery, milder treatment and even reduces the mortality by breast cancer with as much as e.g. 20 % in Sweden [3]. Using mammography, tumours can be detected while they're still too small to be felt and up to 70 % of all breast cancer occurrences are detected by mammography [3]. About 80 % of breast cancer diagnoses happen after the age of 50 and therefore in Sweden the screening is a free and voluntary service offered to all women of the ages 40-74 every 18-24 months [3]. There are however a few drawbacks of mammography, aside from the physical and psychological pain and discomfort, such as false positives, where a harmless change in the breast is classified suspect leading to further investigation and unnecessary worry [3]. Another issue is that it is hard to identify tumours in dense breasts from a x-ray image, especially with younger women [3]. There are also some kinds of tumours that are less visible in images and are therefore sometimes missed [3].

2.3.2 Complementary Methods

MRI, CT and PET are the most common complementary screening methods, most often applied when a suspicious mass have been detected using mammography. MRI uses strong, non-ionizing magnetic fields for imaging and if given the indication that cancer might have evolved, MRI can be used for further examination [3, 5]. Breast MRI is the most sensitive screening method for both invasive and non-invasive cancers and the use of MRI is increasing due to its reliability [14]. It is especially becoming the go-to imaging method for women with dense breast or those with an intermediate to high risk of developing breast cancer [5, 14]. MRI is however a very expensive screening method and many radiologists still lack the expertise to fully interpret the results, which is why it is not yet widely used [5, 14].

CT uses x-rays to create cross-sectional images [5]. The detectors encircle the whole body and measures the projections from multiple angles [5]. CT scanners can resolve objects less than 1 mm in size [15]. PET measures the radioactivity caused by decay of an injected radioactive labelled molecule [16]. When the injected radiotracers decays it emits positrons, which travels a short distance before colliding with electrons, producing two γ-rays [16]. It is these γ-rays that are detected by the PET scanners, and out of which detailed images are recreated of the radiotracer distribution in the body [16]. In similarity with CT, images are created using detectors encircling the body [5, 11]. PET scans often appear blurry compared to MRI

and CT, due to the low amount of photons that can be measured during an imaging session [15]. Another reason for this is that PET scanners cannot correctly resolve objects less than 4-5 mm, and in practise it is actually closer to 10 mm [15].

Palpation is the non-technical method of simply feeling through the breast with ones fingers [3]. Another method is ultrasound, which is commonly used as a complementary screening to mammography [3]. All of the above are non-invasive examination options. If a suspect change in the breast is discovered with any image diagnostics, a biopsy of a tissue sample can be taken to be examined in a microscope [3].

2.4 Microwave Tomography

The research and applications of medical imaging is increasing due to unique characteristics such as it being an non-invasive method with possibly high sensitivity and specificity, together with the wide applicability range, and microwave tomography (MT) is no exception [6]. It is becoming a recognized new screening method worldwide [17]. MT systems typically operate with frequencies between 500 MHz and 3 GHz and uses scattered electric field data to reconstruct dielectric distributions [5].

At microwave frequencies there has been a proven contrast in the dielectric properties between different kinds of tissue, especially adipose, fibroglandular and malignant, which strongly motivates the use of MT in breast cancer detection [17]. For a low water-content tissue such as breast tissue, the contrast between healthy tissue and malignant can be in the range from 10 % up to as high as 400 % [6]. However, too large of a property contrast has been a hurdle for MT and kept it at the developing stage [18]. Otherwise, MT meets several of the market demands, such as being harmless, user-friendly, accurate and economical, the downsides being that the reconstruction requires extensive computational time [17].

It is somewhat important to differ between tomographic imaging and projection imaging, such as mammography. Tomographic imaging utilizes data collections from multiple angles to reconstruct a cross-sectional image, while projection imaging uses direct transmitted radiation [7]. Tomographic imaging is therefore more computationally heavy but it also has the ability to illustrate distributions along the propagation direction and thereby presents the possibility to capture the relative depth between objects, see the distinctions in Figure 2.2 [7].

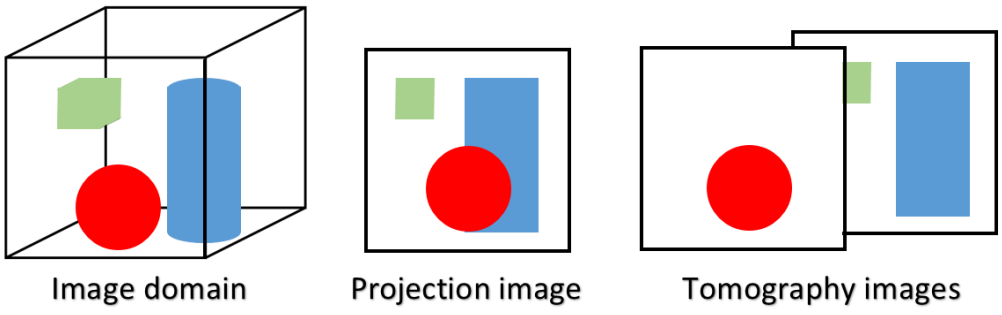

Figure 2.2: Illustration of the difference between projection imaging and tomographic imaging.

2.4.1 Physical Measurement System

In order to reconstruct 2D images, a set of 16 monopole antennas, each working as both transmitters and receivers, are placed with even spacing in a circle of radius $r = 7.62$ cm, starting at $-\pi/2$ counting clockwise, see the exact positions in Figure 2.3 and Table 2.1 [5, 7]. Monopole antennas have numerous advantages, including that their small profile only slightly disturbs the the field patterns [6]. In sequence they transmit an electromagnetic wave that propagates through the tissue of the breast. The measurements are collected by the remaining 15 antennas. Those close to the radiator primarily measure the waves reflected off tissue surfaces while the opposing antennas primarily pick up the transmitted waves [7]. Dielectric properties of the transilluminated tissues can be gathered from the multi-view scattered intensity and phase distributions [6].

The antennas are placed inside a cylindrical tank of radius $r = 13.95$ cm, filled with a biologically sterile glycerine and water based coupling medium [6, 7]. A highly attenuating coupling medium effectively diminishes field interactions between structures such as surface waves and unwanted effects from multi-path signals, making sure the received signals are dominated by waves that have propagated through the image domain [6, 7]. The coupling medium also works to lowers the contrast between the breast and surrounding by having dielectric properties closer to that of breast tissue than air [7]. The mixing ratio should be adjusted to best fit the breast composition; a volume percentage of 80 % glycerine and 20 % water is often used for dense breasts, while a fattier breast is better matched with 86 % glycerine and 14 % water [6, 7]. A detailed description of measurement system can be found in [6, 7].

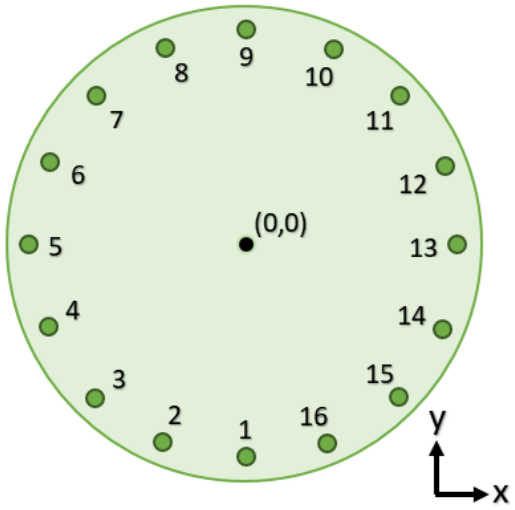

Figure 2.3: The illustrated numbering and placing of the 16 antennas.

Antenna	x [m]	y [m]
1	-1.3998e-17	-0.0762
2	-0.02916	-0.0704
3	-0.053882	-0.053882
4	-0.0704	-0.02916
5	-0.0762	9.3318e-18
6	-0.0704	0.02916
7	-0.053882	0.053882
8	-0.02916	0.0704
9	4.6659e-18	0.0762
10	0.02916	0.0704
11	0.053882	0.053882
12	0.0704	0.02916
13	0.0762	0
14	0.0704	-0.02916
15	0.053882	-0.053882
16	0.02916	-0.0704

Table 2.1: The numerical numbering and placing of the 16 antennas.

2.5 Electromagnetics of Biological Tissue

In order to solve the forward problem of tomography, which requires extensive computation, some understanding of fundamental electromagnetics is required [17]. Throughout the following sections the convention $\bar{x}, \bar{\bar{x}}$ is used to represent vector and matrix notation respectively.

2.5.1 Electromagnetic Field Theory

The physical interactions between fields, fluxes and material properties can be described by Maxwell's equations and the complex form of these in the frequency domain are expressed as,

$$\bar{\nabla} \cdot \bar{D} = \rho \tag{2.1a}$$
$$\bar{\nabla} \cdot \bar{B} = 0 \tag{2.1b}$$
$$\bar{\nabla} \times \bar{E} = -i\omega\bar{B} \tag{2.1c}$$
$$\bar{\nabla} \times \bar{H} = \bar{J} + i\omega\bar{D}, \tag{2.1d}$$

where $\bar{D}$ is the displacement field, $\bar{B}$ is the magnetic flux density, $\bar{E}$ is the electric field, $\bar{H}$ is the magnetic field and $\bar{J}$ is the current density [19]. Looking at the parameters i is the imaginary unit, ω is the frequency and ρ is the charge density [19].

$\epsilon = \epsilon_0\epsilon_r$ is the permittivity (free-space and relative) and $\mu = \mu_0\mu_r$ is the permeability [19]. From here on $\mu_r = 1$, since all relevant materials are non-magnetic. By using the following constitutive relationships,

$$\bar{D} = \epsilon\bar{E} \tag{2.2a}$$
$$\bar{B} = \mu\bar{H} \tag{2.2b}$$
$$\bar{J} = \sigma\bar{E}, \tag{2.2c}$$

the displacement field, magnetic flux and current density in Equation (2.1) can be substituted [5, 19]. This gives a new form for the Maxwell's equations when there is no free charge nor current present,

$$\bar{\nabla} \cdot (\epsilon\bar{E}) = 0 \tag{2.3a}$$
$$\bar{\nabla} \cdot (\mu\bar{H}) = 0 \tag{2.3b}$$
$$\bar{\nabla} \times \bar{E} = -i\omega\mu\bar{H} \tag{2.3c}$$
$$\bar{\nabla} \times \bar{H} = i\omega\epsilon\bar{E}. \tag{2.3d}$$

Taking the curl of Equation (2.3a) and inserting it into Equation (2.3b) results in,

$$\bar{\nabla} \cdot (\bar{\nabla} \cdot \bar{E}) - \bar{\nabla}^2\bar{E} = k^2\bar{E}, \tag{2.4}$$

where $k^2 = \omega^2\mu\epsilon$ is the squared wavenumber, representing energy absorbing in material [5]. Remembering $\mu_r = 1$ it becomes

$$k^2 = \omega^2\mu_0\epsilon + i\omega\mu_0\sigma. \tag{2.5}$$

Inserting $\bar{\nabla} \cdot \bar{E} = 0$ (zero charge density) into Equation (2.4) results in the Helmholtz equation,

$$\bar{\nabla}^2 \bar{E} - k^2 \bar{E} = 0, \tag{2.6}$$

which is a necessary equation in order to solve the forward problem in inhomogeneous image domains, described in Section 2.6 [5].

2.5.2 Scattering

The Helmholtz Equation (2.6) can be divided into incident field, $\bar{E}_{inc}$, and scattered field, $\bar{E}_{scat}$, such that,

$$\bar{E}_{tot} = \bar{E}_{inc} + \bar{E}_{scat}. \tag{2.7}$$

This is useful when an incident field hits a scattering object, as seen in Figure 2.4 [5]. The problem of determining the scattered electric field due to the object, when the incident field and dielectric properties of the background, ϵ_b, σ_b, are known, then becomes Equation (2.7). This is done in a bounded region $V \subset \mathbb{R}^d, d = 2, 3$ [5].

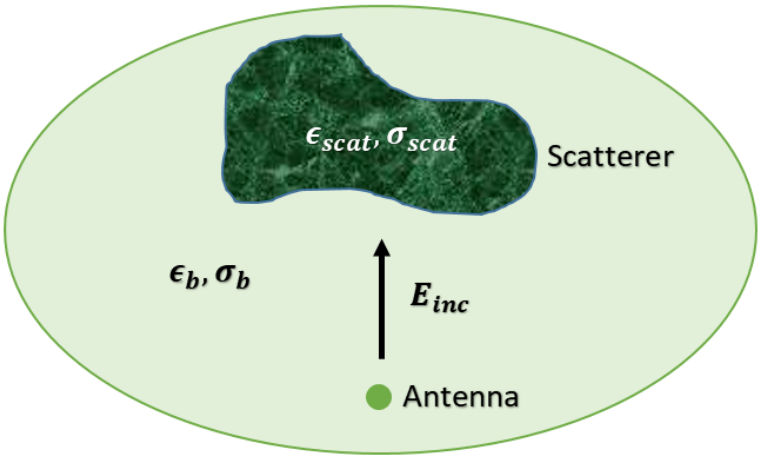

Figure 2.4: Domain of interest for determining the scattering field of an object.

2.5.3 Single-pole Cole-Cole Equation

The combination of permittivity and conductivity is often used to describe several dielectric properties in materials, such as electric loss and polarizability [7]. Said properties are also frequency dependent, which is why relaxation models have been developed to ease the understanding of that relation [7]. This knowledge is fundamental e.g. when creating phantom studies and tissue-mimicking mixtures. Cole-Cole models are relaxation models commonly used as physics-based compact representations of wideband frequency-dependent dielectric properties to describe the relaxation of said properties in polymers [20]. It has been proven that in the frequency range 0.5-20 GHz a single pole Cole-Cole model,

$$\epsilon(\omega) = \epsilon_\infty + \frac{\Delta\epsilon}{1 + (i\omega\tau)^{1-\alpha}} + \frac{\sigma_s}{i\omega\epsilon_0}, \tag{2.8}$$

is sufficient to fit the dielectric properties of tissue [20]. The Cole-Cole parameters ϵ_∞, $\Delta\epsilon = \epsilon_s - \epsilon_\infty$, σ_s, τ and α are estimated from experimental data [20]. The single pole model consists of a real and an imaginary part,

$$\epsilon(\omega) = \epsilon_r\epsilon_0 + i\frac{\sigma}{\epsilon_0\omega} = Re(\epsilon) + iIm(\epsilon). \tag{2.9}$$

The real part is the frequency dependent dielectric constant and the imaginary part is the frequency dependent dielectric loss, which can be converted into the effective conductivity $\sigma_{eff}(\omega) = \omega\epsilon_0$.

2.6 Reconstruction Algorithm

The fast 2D electromagnetic reconstruction algorithm developed by Hosseinzadegan [5], can be divided into two main parts: *the forward solution* and *the inverse problem*. The forward solution predicts the electromagnetic propagation in a domain where the initial conditions, boundary conditions and the dielectric parameters are known. The inverse problem uses a model for scattering during electromagnetic propagation to recover the dielectric properties of a domain. Its main objective is to minimize the difference between measured data and the computed forward solution. The algorithm updates the dielectric properties in each iteration until the convergence criteria is fulfilled. The inverse problem requires these computationally expensive, iterative, optimization algorithms when applied to MT, due to the large property contrasts between tissues. An universal overview of the reconstruction algorithm is given in Figure 2.5.

The forward solution is calculated in each iteration of the reconstruction algorithm, making it the main computational load. Therefore the forward solution algorithm plays an important role in the total computational complexity and time. The fundamental electromagnetic equations described in Section 2.5.1 can be solved using multiple different numerical methods, including the discrete dipole approximation, finite-difference time-domain and finite element methods.

2.6.1 Discrete Dipole Approximation

The discrete dipole approximation (DDA) is built on the idea of replacing an object with an array of dipoles and can be used to calculate scattering properties for an arbitrarily shaped object [5]. According to Hosseinzadegan [5], the image domain, D, is represented by an array of dipoles in n equally spaced cells, D_i, such that,

$$D = \lim_{n\to\infty} \bigcup_{i=1}^{n} D_i. \tag{2.10}$$

An electrical line source is used to create the electrical incident field $\bar{E}_{inc}$. The descriptions of the incident field, scattered electrical field, $\bar{E}_{scat}$, and the total electrical field, $\bar{E}_{tot}$, at any dipole location, $\bar{r}_i$, a distance $\bar{R}_i$ from the transmitting antenna,

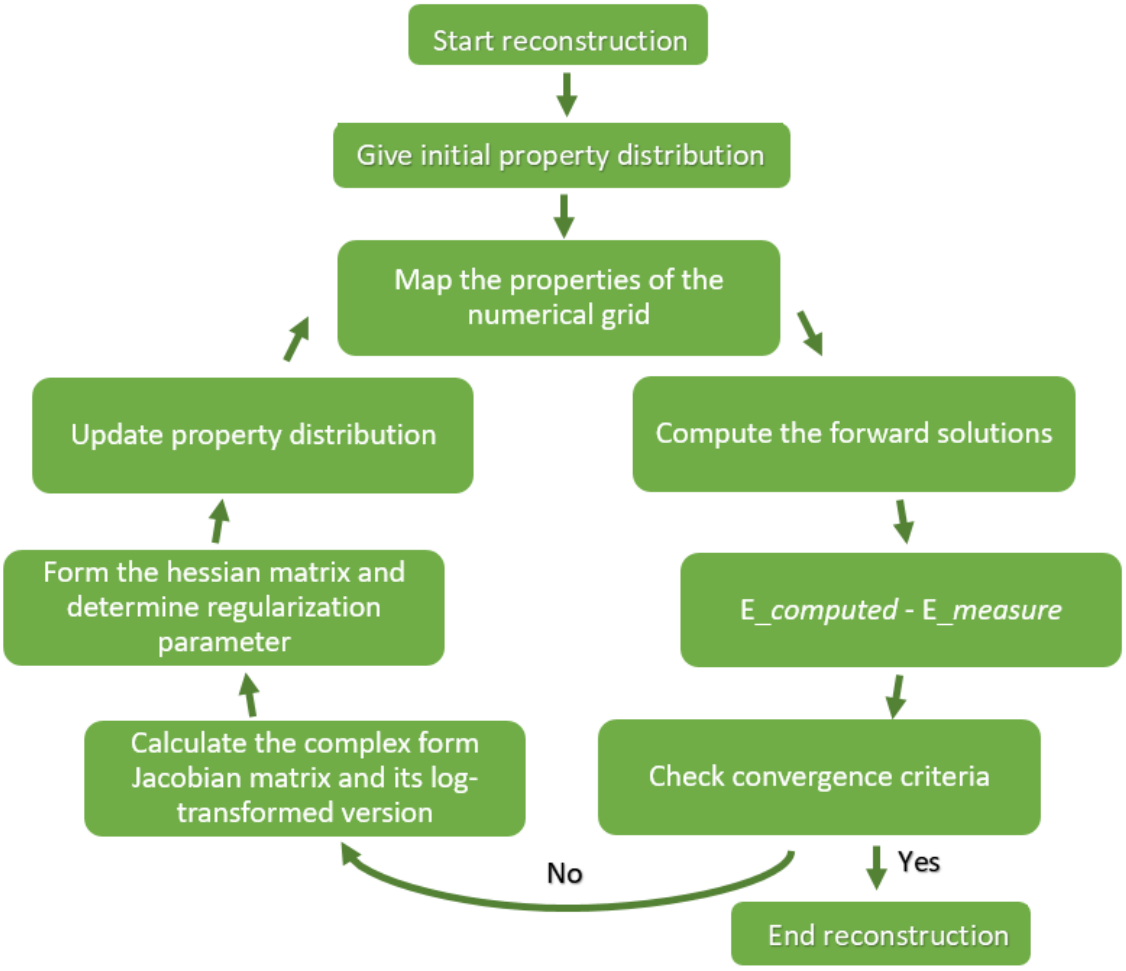

Figure 2.5: An universal overview of the reconstruction algorithm.

is represented as,

$$\bar{E}_{inc}(\bar{r}_i) = \frac{I_0 \omega \mu_0}{4} H_0^2(k_b) \bar{R}_i \tag{2.11a}$$

$$\bar{E}_{scat}(\bar{r}_i) = \sum_{j=1 j \neq i}^{N} \bar{\bar{G}}_{ij} \bar{P}_j \tag{2.11b}$$

$$\bar{E}_{tot}(\bar{r}_i) = \bar{E}_{inc}(\bar{r}_i) + \bar{E}_{scat}(\bar{r}_i). \tag{2.11c}$$

Here the constants I_0, ω, μ_0 and k_b are the current amplitude, frequency, free-space permeability and background wavenumber respectively. H_0^2 is the zero-order, second kind Hankel function. $\bar{\bar{G}}$ is the dipole interaction matrix, originating from the Green's function for the 2D Helmholtz equation, describing the interaction between two dipoles located at r_i and r_j respectively,

$$\bar{\bar{G}}_{ij} = \frac{-i}{4} H_0^2(k_b \bar{r}_{ij}). \tag{2.12}$$

Finally, $\bar{P}$ is the polarization, representing the, assumed to be constant, material properties at each dipole location. Furthermore, the polarization is proportional to

the free-space permittivity, ϵ_0, the susceptibility χ and $\bar{E}_{tot}$ on a macroscopic level (Eq. (2.13a)). It is also proportional to the number of molecules per unit volume, N, ϵ_0, the polarizability term, α, and the microscopic electric field sensed by each molecule, $\bar{E}_{loc}$, on a microscopic level (Eq. (2.13b)),

$$\bar{P} \propto \epsilon_0 \chi \bar{E}_{tot} \tag{2.13a}$$

$$\bar{P} \propto N \epsilon_0 \alpha \bar{E}_{loc}. \tag{2.13b}$$

A full description of the 2D DDA algorithm can be found in [5].

2.6.2 Finite-Difference Time-Domain Method

The finite-difference time-domain method (FDTD) is a frequently used numerical method in microwave problems [5]. It is a grid-based, time-domain, numerical analysis technique able to cover a wide range of frequencies in a single simulation run, often used in computational electrodynamics [21, 22]. This differential numerical model solves the Maxwell equations, see Equation (2.1), on a mesh, without any physical approximation, includes the effects of transmission, reflection, absorption and scattering, and computes $\bar{E}$ and $\bar{H}$ in all three spatial dimensions [21, 22]. The developed FDTD algorithm used is an iterative gradient-descent based model and, similarly to the DDA algorithm, computes the forward solution in each iteration and uses the residuals between computed and measured data to adjust the computational domain [7, 23]. Said domain is a Debye relaxation model, whose adjustable parameters are given in the single-pole Cole-Cole Equation (2.8) [7, 23]. A full description of the FDTD algorithm can be found in [24].

2.6.3 Finite Element Method

The finite element method (FEM) is a popular numerical solver used in forward problem solving where the principle is to divide the image domain into smaller domains in the shape of triangles in 2D or tetrahedrons in 3D [25]. FEM is a great method to use when dealing with complex, arbitrary geometries. It has the power to finely disceretize oddly shaped objects and surrounding areas, all while keeping the homogeneous zones more coarsely mapped without losing accuracy. FDTD and FEM are comparable in 2D, but in 3D FEM usually requires a lot more memory and CPU time [5]. FEM uses linear polynomials on each of the meshes to express the electrical field in the domain, and a finer mesh leads to more equations [5]. The computational complexity therefore grows the finer the mesh is, but that is also necessary to generate an image with a high accuracy in the electric field distribution, and there are several methods to efficiently reduce the computational time. The Dartmouth research group have successfully been using FEM to calculate the electric field with their clinical imaging system to reconstruct images in near real time [5, 26]. It is an iterative Gauss-Newton based FEM algorithm, consisting of two main parts: 50 iterations using a Levenberg-Marquardt mehtod, followed by 20 iterations using a Tikhonov regulation [7, 27, 28]. A full description of their FEM algorithm can be found in [28].

3
Methods

In order to validate and evaluate the accuracy of the 2D DDA algorithm, it had to be experimentally tested and compared with the corresponding results from other forward solutions. The DDA forward solution and the reconstruction algorithm are written in MATLAB version 2022b, COMSOL Multiphysics version 5.6 is used to implement a FEM model and the FDTD forward solution is implemented in C++. There are two primary areas of investigation, the first is comparing the calibrated amplitudes and calibrated phases in the forward solutions, and the second is creating reconstructions based on the calibrated data. Throughout this thesis the term calibrated will refer to the subtractions of homogeneous background data from the specific forward solution,

$$\bar{E}_{cal} = \bar{E}_{sim} - \bar{E}_{bg}. \tag{3.1}$$

Most experiments used quite simple geometry, described in detail in their respective sections below, in order to isolate and easily test the characteristic of interest. The physical setting described in Section 2.4.1 lays the ground for all experimental work performed in this thesis. In all simulations, the placing of the antennas is kept constant in accordance with Table 2.1. If nothing else is specified, then for all computations of the forward solution using the DDA algorithm or COMSOL, the grid and mesh size was 3.906 mm while the FDTD algorithm had a grid size of 1.0 mm. These were chosen based on previous work. The background permittivity was $\epsilon = 25$ and the background conductivity was $\sigma = 1.4$ for all solutions. Remembering the materials are non-magnetic, $\mu_r = 1$ also applies in all cases. The background values, as well as the frequency $f = 1.3$ GHz, were chosen so it would be possible to compare and validate the results to previous work performed with the system and algorithms in [5, 6, 7, 17].

DDA
The DDA algorithm is the main objective of the thesis and the algorithm to be evaluated. The DDA algorithm used is the one described in [5] and implemented in MATLAB.

COMSOL
COMSOL Multiphysics was used to simulate electric field data. Electromagnetic wave simulations were performed in the frequency domain. The antennas were put in as Line Current (Out-of-Plane) electrical line sources at the given positions. A parametric sweep (i=1-16) simulation was run, where a rectangle function (limits ± 0.5) was used to alternate the antennas from being transmitters and receivers. The

current was set to 0.01 A. The generated output from COMSOL had to be divided by 15 in order to match the E-field amplitude and phase generated by the DDA and FDTD algorithms. This was caused by the uncertainty of which amplitude to give the input current.

FDTD

The FDTD algorithm described in [23] was implemented in C++ and used to generate forward solutions to be compared to the ones generated using the DDA algorithm and COMSOL.

Phase Shift

The phase shifted multiple times for the microwaves while propagating through the image domain, alternating between -180° and 180°. For this reason a phase shift had to be introduced. The phase propagation through the image domain is illustrated in Figure 3.1a and the difference between the phase before and after the shift is illustrated in Figure 3.1b. This was necessary to get the correct calibrated phase, which could then be used in the reconstructions.

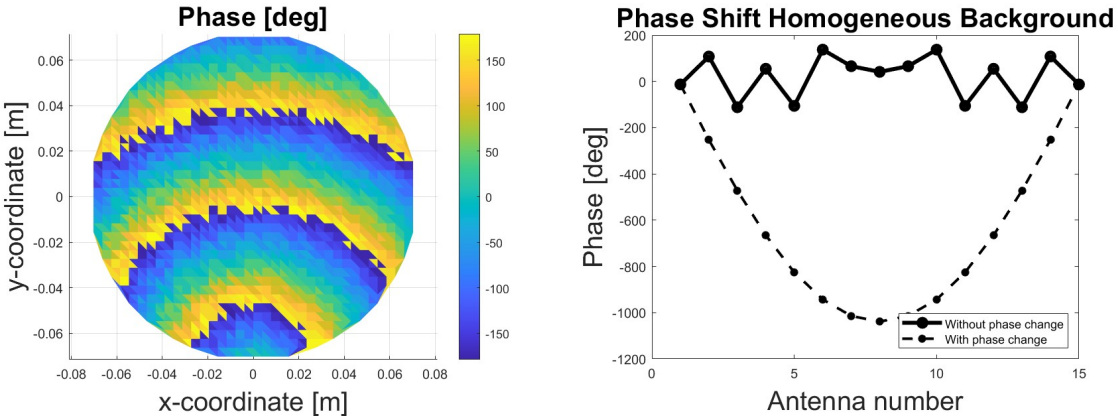

(a) Phase propagation through the image domain

(b) The difference before and after applying phase shift

Figure 3.1: Illustration of phase propagation and the effect of applying phase shift.

3.1 Convergence Study

First the grid and mesh sizes had to be evaluated to be fine enough. This was done with a simple convergence test where the grid and mesh sizes were varied. Using 3.906 mm, the given grid size in the DDA algorithm, as the starting point, that original mesh size was halved, doubled and multiplied by ten in COMSOL for the FEM model to 1.9 mm, 7.8 mm and 39 mm respectively. In MATLAB the size was halved both once and twice for the DDA model to 2 mm and 1 mm respectively, in order to compare it to the 1 mm grid size of the FDTD algorithm. Increasing the grid size for the DDA model was deemed unnecessary based on the results from COMSOL and previous results found in [17].

3.2 Size Evaluation

To see the dependence of an object's size for detection, several circles placed in Origo were used, see the general setup in Figure 3.2. The radius of the circles range from $r = 5$ mm to $r = 65$ mm, with steps of 10 mm, i.e. the radius ranged from almost homogeneous background to almost the full size of the physical setup of the antennas, see Table 3.1. Two cases were performed: first the permittivity was lowered to that of adipose tissue, $\epsilon = 15$, $\sigma = 0.9$, simulation IDs S1-S8 in Table 3.1. In the second run the dielectric properties were increase to that of glandular tissue, $\epsilon = 35$, $\sigma = 1.7$, simulation IDs S9-S16. This to mimic cases of both adipose and dense breast and to be able to compare the effect of both lowered and increased dielectric values compared to the background. An additional radius of $r = 30$ mm was added due to the change in behaviour for the adipose circles around that size. S1-S16 in Table 3.1 were simulated with both DDA and COMSOL. S2, S7, S10 and S15 were also simulated with FDTD to generate the forward solution. These were chosen as to include both a smaller and a larger object with lower and higher dielectric properties compared to the background respectively.

Table 3.1: The radii used in the size evaluation and their respective simulation ID.

Simulation	S1	S2	S3	S4	S5	S6	S7	S8
ϵ	15	15	15	15	15	15	15	15
σ	0.9	0.9	0.9	0.9	0.9	0.9	0.9	0.9
r [mm]	5	15	25	30	35	45	55	65
Simulation	S9	S10	S11	S12	S13	S14	S15	S16
ϵ	35	35	35	35	35	35	35	35
σ	1.7	1.7	1.7	1.7	1.7	1.7	1.7	1.7
r [mm]	5	15	25	30	35	45	55	65

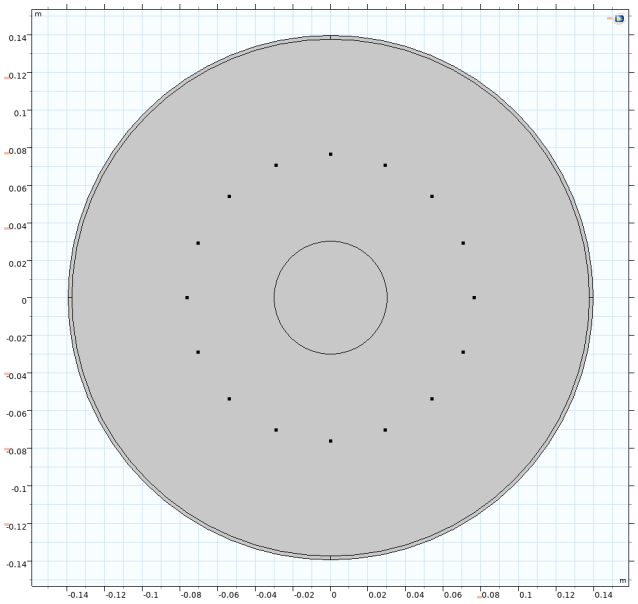

Figure 3.2: The general setup used in the size and dielectric properties evaluations.

3.3 Dielectric Properties Evaluation

A small circle with radius 25 mm centered in Origo (Fig. 3.2) was used for this evaluation, the size choice was based on the results from the size evaluation in Section 3.2. The values tested can bee seen in Table 3.2. A small convergence study was performed; in the first four simulations, Di1-Di4, σ is kept constant and in the second half, Di5-Di8, ϵ is kept constant in accordance with their respective background values. This study was to evaluate the dependence of the permittivity and the conductivity separately.

Table 3.2: The dielectric values used in the dielectric properties evaluation and their respective simulation ID.

Simulation	Di1	Di2	Di3	Di4	Di5	Di6	Di7	Di8
ϵ	5	15	35	45	25	25	25	25
σ	1.4	1.4	1.4	1.4	0.6	1.0	1.8	2.2
r [mm]	25	25	25	25	25	25	25	25

3.4 Concentric Circles Evaluation

The use of two concentric circles, both centered in Origo, was a step to a slightly more realistic breast model, see Figure 3.3. The outer circle mimicked adipose tissue with $\epsilon = 15$, $\sigma = 0.9$, while the inner circle mimicked fibroglandular tissue with $\epsilon = 35$, $\sigma = 1.7$. The radius of both circles was varied in accordance with Table 3.3.

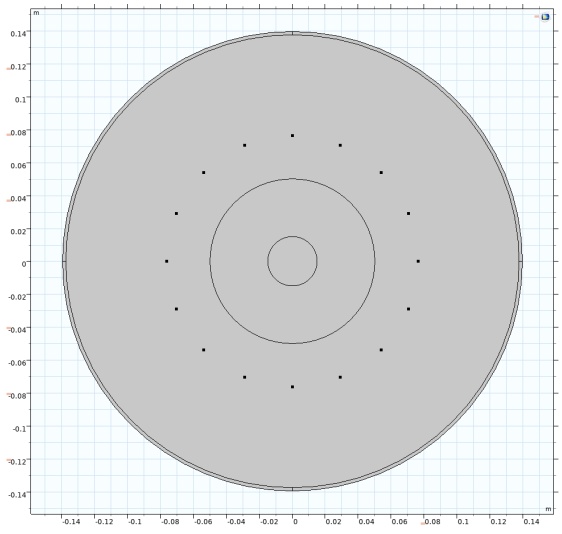

Figure 3.3: The general setup used in the concentric circles evaluation
.

Sim.	**Outer [mm]**	**Inner [mm]**
CC1	40	10
CC2	40	15
CC3	40	20
CC4	40	25
CC5	40	30
CC6	50	10
CC7	50	15
CC8	50	20
CC9	50	25
CC10	50	30
CC11	60	10
CC12	60	15
CC13	60	20
CC14	60	25
CC15	60	30

Table 3.3: The radii used in the concentric circles evaluation and their respective simulation ID.

3.5 Reconstructions

The reconstruction algorithm used is the one described by Hosseinzadegan [5]. It takes as input the E-field generated by either of the three forward solvers DDA, COMSOL or FDTD. Then when running the reconstruction iterations, the algorithm uses DDA as the forward solution to iterated over, regardless of the initial forward solution used to generate the E-field.

3.5.1 Simulations

The models S2, S7, S10 and S15 in Table 3.1 were reconstructed using the forward solutions from DDA, COMSOL and FDTD respectively to generate the E-fields. These simulations were chosen to include both small and large objects with higher and lower dielectric properties than the background. Additionally, the DDA generated fields for the smaller object for both adipose and fibroglandular dielectric properties (S2, S10), were reconstructed with 50 iterations to see if more iterations generates a better result.

3.5.2 MRI Phantoms

An exception to the simple geometries were done only with the use of anatomically-realistic MRI-derived numerical breast phantoms, provided by the UWCEM Numerical Breast Phantom Repository [29]. Unfortunately the open source voxel data was not compatible with COMSOL at this stage, which would have been the preferred comparison to make. However, the voxel data was compatible with both the DDA and FDTD algorithms. There are nine available phantoms divided into four classes: *Mostly Fatty, Scattered Fibroglandular, Heterogeneously Dense* and *Very Dense* depending on their radiographic density defined by the American collage of Radiology [29]. Class 1 is < 25 % glandular tissue, class 2 is 25-50 % glandular tissue, class 3 is 51-75 % and the fourth class is > 75 % glandular tissue [29]. For this thesis a breast from the third class was used, with ID 062204.

2D Coronal Plane

To get a cross section of the breast, the voxel data was transformed according to E. Zastrow et al. [20], and the 145th level in the x-direction was extracted from the 3D-matrice. Each voxel is $0.5 \times 0.5 \times 0.5$ mm^3, so to get the xy-position for each voxel when the phantom is centered in Origo, see Figure 3.4, half of the total amount of rows or columns is subtracted from the voxel's index-position (ix, iy) respectively and the sum is multiplied with 0.0005, see Equation 3.2. Interpolation was then used to capture the most representative property distributions when mapping the MRI image to the DDA and FDTD grid, since they were of larger grid sizes.

$$\begin{aligned} x &= 0.0005(ix - rows/2) \\ y &= 0.0005(iy - cols/2) \end{aligned} \tag{3.2}$$

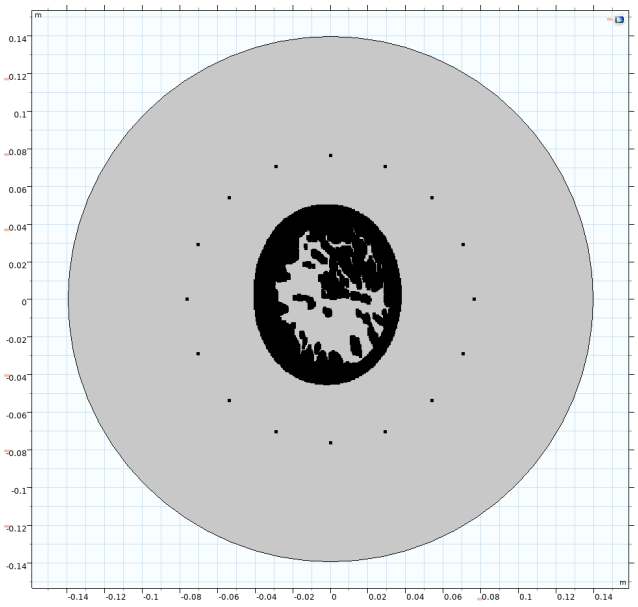

Figure 3.4: The general setup used for the MRI phantom.

Dielectric Properties

UWCEM provides the data in two files: *mtype* and *pval*. The former is an identifier for each tissue and the latter gives the dielectric properties information for each voxel. Voxels representing normal breast tissue or subcutaneous fat are assigned a value $p \in [0, 1]$, where a lower p represents a lower dielectric property value and a p close to 1 represent a high value. All other voxel's p-values are set to zero. In order to get the dielectric properties both mtype and pval are needed. For each tissue type there is an upper and lower boundary for the permittivity and conductivity respectively. These boundaries have been calculated using the single pole Cole-Cole model (Eq. (2.8)) using the experimental input data from E. Zastrow et al. [20], see Table 3.4.

Table 3.4: The eight wideband dielectric properties for the limits of each of the seven tissue types.

Limit	ϵ_∞	$\Delta\epsilon$	τ **(ps)**	α	σ_s **(S/m)**
Upper/Fibroglandular-1	1.000	66.31	7.585	0.063	1.370
Fibroglandular-1/2	6.151	48.26	10.26	0.049	0.809
Fibroglandular-2/3	7.821	41.48	10.66	0.047	0.713
Fibroglandular-3/Transitional	9.941	26.60	10.90	0.003	0.462
Transitional/Adipose-1	4.031	3.654	14.12	0.055	0.083
Adipose-1/2	3.140	1.708	14.65	0.061	0.036
Adipose-2/3	2.908	1.200	16.88	0.069	0.020
Adipose-3/Lower	2.293	0.141	16.40	0.251	0.002

The frequency used is $f = 1.3$ GHz, i.e. $\omega = 2\pi \cdot 1.3 \cdot 10^9$. Equation (3.3) shows how the dielectric values are found given the upper and lower limit of the tissue

together with the p-value for a voxel,

$$\begin{aligned} \epsilon &= p \cdot \epsilon_{upper} + (p-1) \cdot \epsilon_{lower} \\ \sigma &= p \cdot \sigma_{upper} + (p-1) \cdot \sigma_{lower} \\ \alpha &= \epsilon + i\sigma. \end{aligned} \tag{3.3}$$

Phantom Simulations

The original dielectric distributions for MRI phantom with ID 062204 at frequency $f = 1.3$ GHz can be seen in Figure 3.5. The E-field of the MRI phantom was calculated using the forward solution DDA for a grid size of 3.9 mm. FDTD was used to generate the E-field for a grid size of 1 mm. These two cases where then used in the reconstructions algorithm to reconstruct both the permittivity and conductivity distributions.

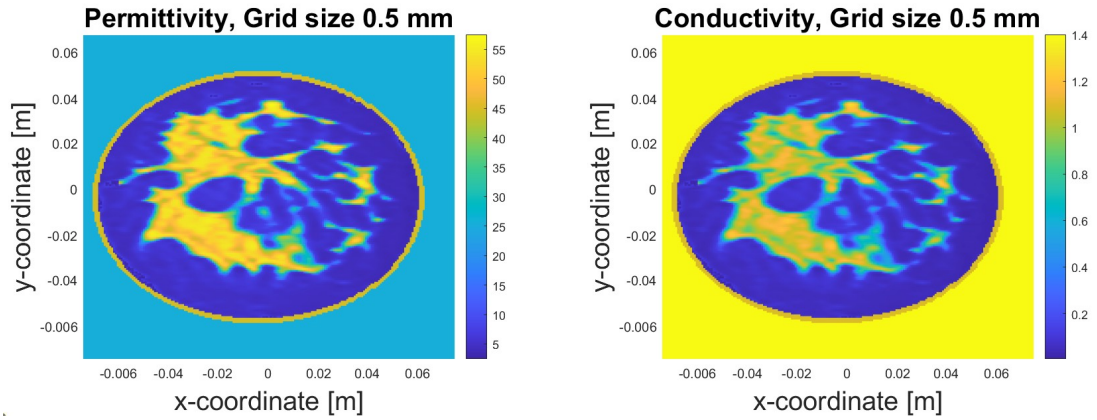

(a) **(b)**

Figure 3.5: Dielectric distributions of MRI phantom with ID 062204.

4
Results

This chapter presents the results from the simulations and reconstructions described in the Methods chapter. The calibrated amplitude is displayed in dB at the neighbouring antennas, and the calibrated phase is displayed in degrees in the same order. When inspecting the amplitude and phase plots the objective is to illustrate whether or not the different forward solutions generate comparable E-field solutions. The general shape of the curves is the main characteristic of interest, including the location and magnitude of peaks, if the curve is concave or convex and the scale. Take note to the amplitude and phase scales when comparing the different simulations to one another. Heatmaps showing the root mean square error (RMS) between the DDA and COMSOL solutions were also generated to more easily compare the calibrated data between plots. When inspecting the reconstructions the shape and dielectric values should be compared to the target shape and values.

4.1 Convergence Study

The results from the convergence study can be seen in Figure 4.1. COMSOL showed that the mesh size is small enough. Only the magenta curves with a mesh size ten times larger then the original showed a deviating appearance, all other results are perfectly aligned. Decreasing the grid size to 2 mm in the DDA algorithm led to a computational time of 30 min for one iteration of the forward solution, instead of the 98 s it took for the original grid size 3.9 mm. Decreasing it to 1 mm caused the forward solution to break due to the matrix computations being too demanding.

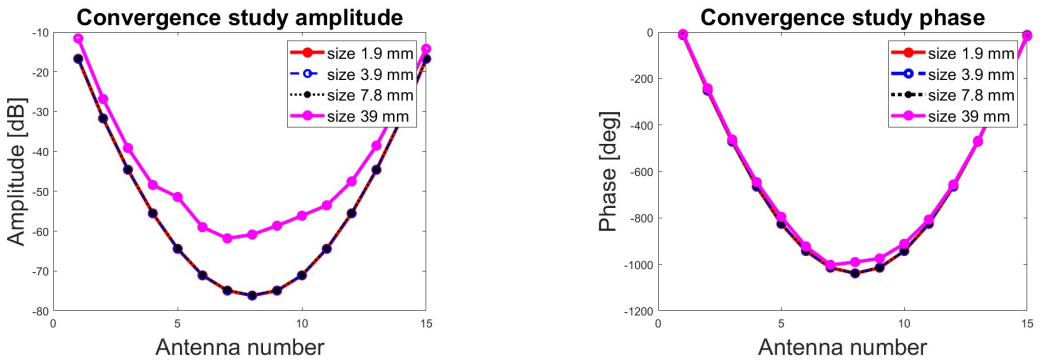

(a) **(b)**

Figure 4.1: The background amplitude and phase for the convergence study in COMSOL.

4.2 Size Evaluation

The results from the size evaluation can be seen in Figures 4.2-4.11. The heatmaps in Figures 4.2-4.3 shows the amplitude RMS and phase RMS respectively between DDA and COMSOL for the adipose and fibroglandular objects of different sizes. There is a clear correlation between larger objects and a larger RMS. This is more prominent for adipose objects with lower dielectric properties compared to the background.

Figure 4.4 shows the calibrated amplitude for an adipose object, corresponding to simulation IDs S1-S8, and Figure 4.5 shows the calibrated amplitude for a fibroglandular object, corresponding to simulation IDs S9-S16. Comparing these plots there is a clear deviation between the DDA and COMSOL solutions for adipose objects (Fig. 4.4), while the fibroglandular curves are comparable for all object sizes (Fig. 4.5), not just the smaller ones. Figure 4.6 shows the calibrated phase for an adipose object, corresponding to simulation IDs S1-S8, and Figure 4.7 shows the calibrated phase for a fibroglandular object, corresponding to simulation IDs S9-S16. The phase curves are highly comparable for both tissue types and for all sizes.

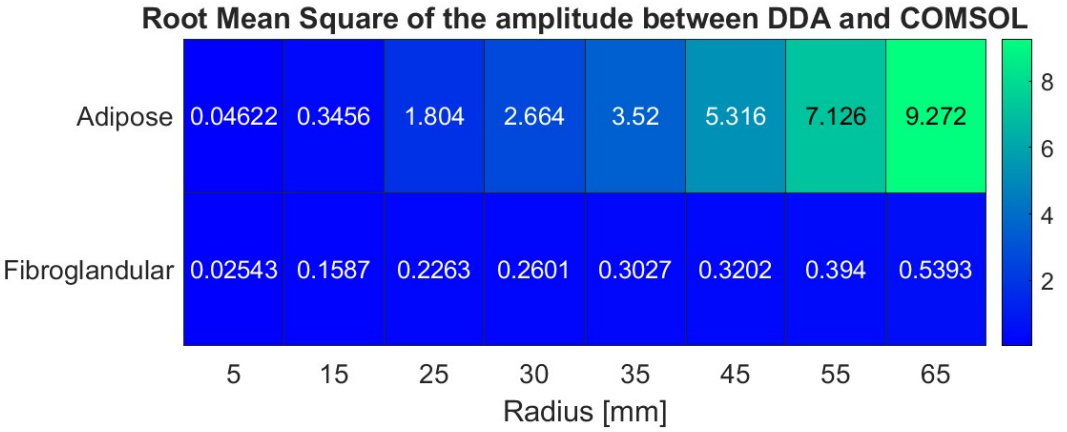

Figure 4.2: Heatmap of the amplitude RMS for the size evaluation.

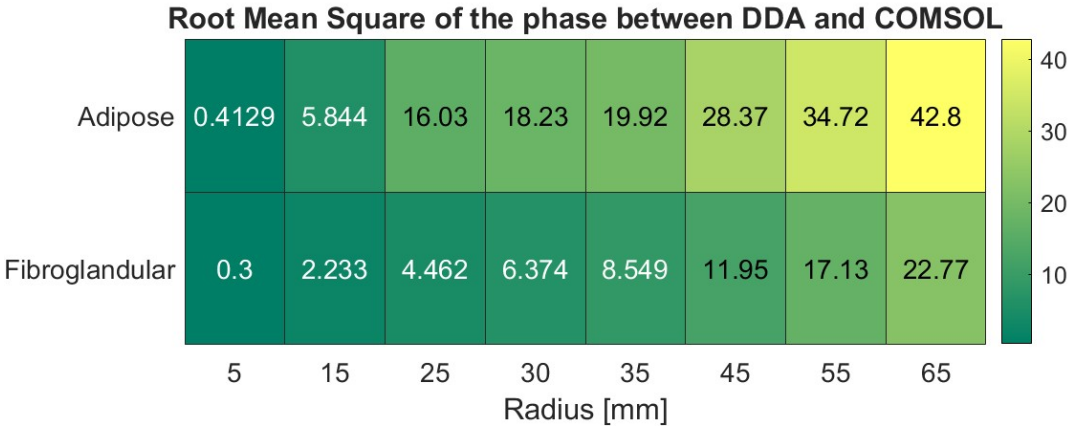

Figure 4.3: Heatmap of the phase RMS for the size evaluation.

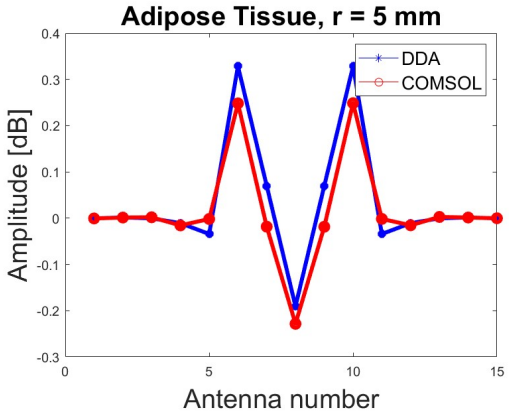

(a) S1

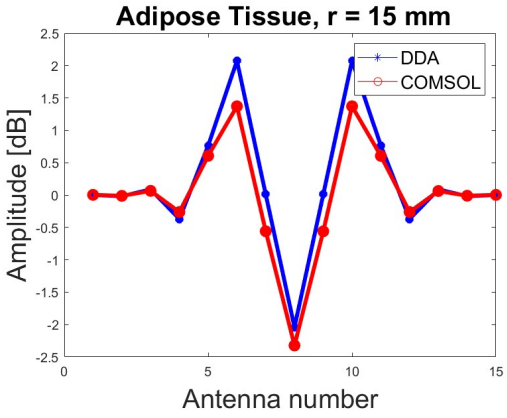

(b) S2

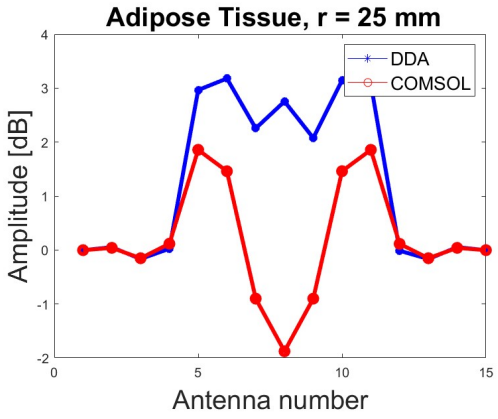

(c) S3

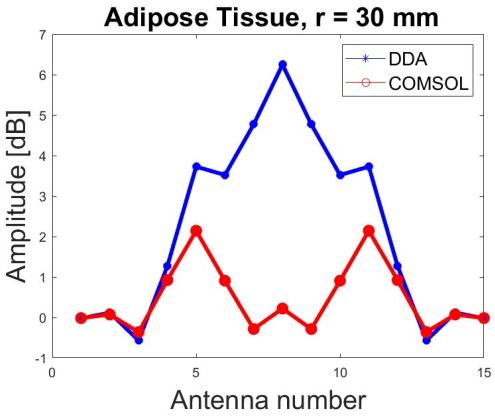

(d) S4

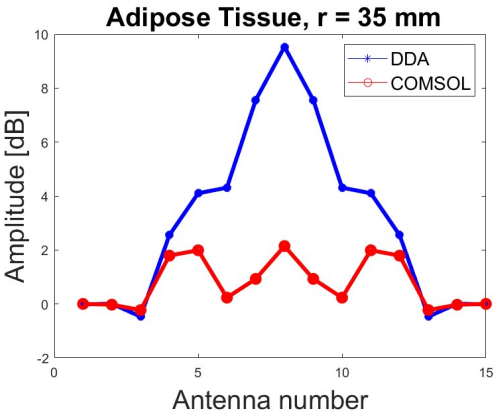

(e) S5

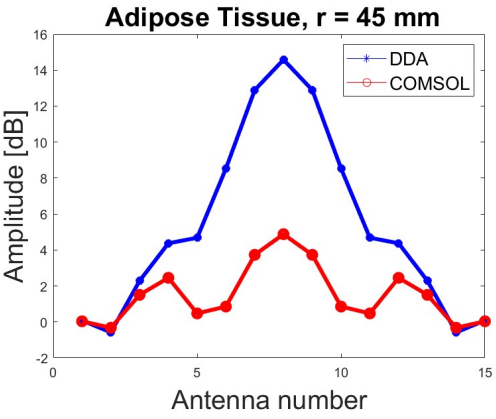

(f) S6

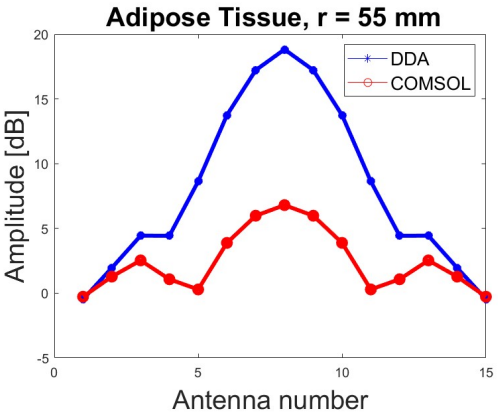

(g) S7

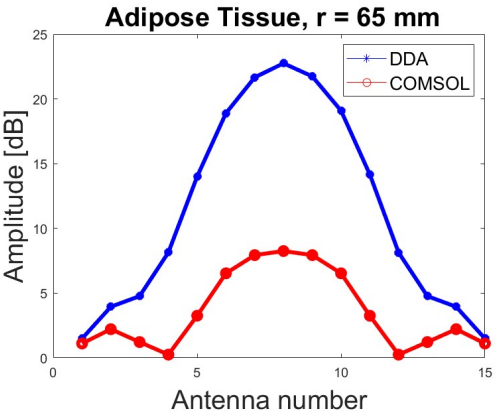

(h) S8

Figure 4.4: Calibrated amplitude for the size evaluation of an adipose object.

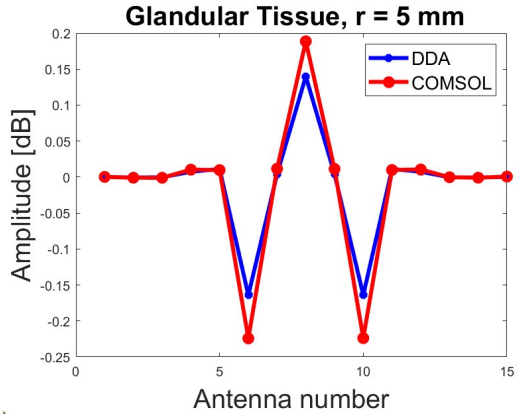

(a) S9

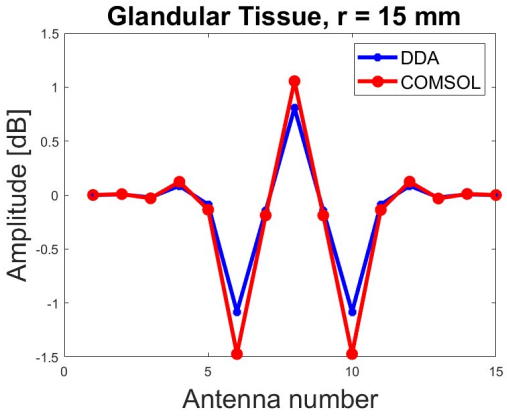

(b) S10

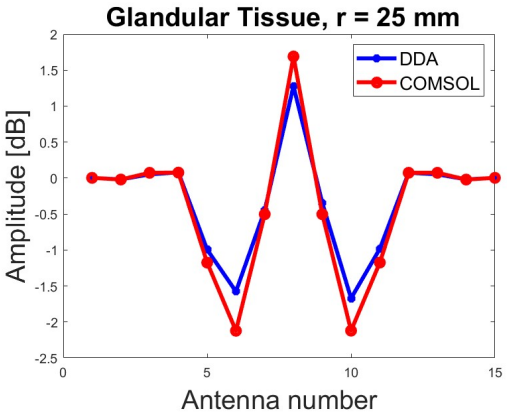

(c) S11

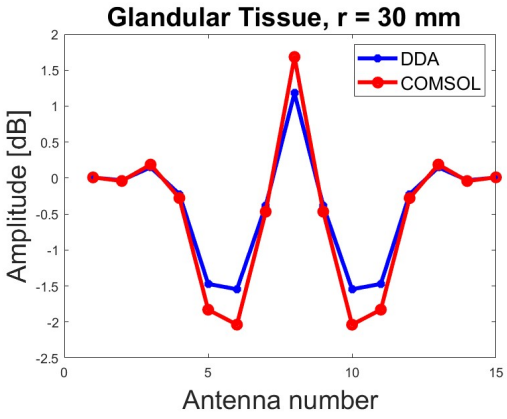

(d) S12

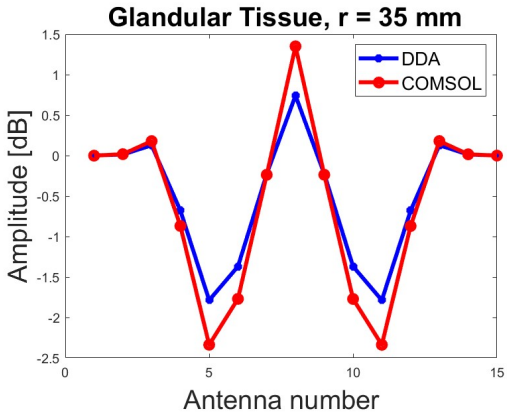

(e) S13

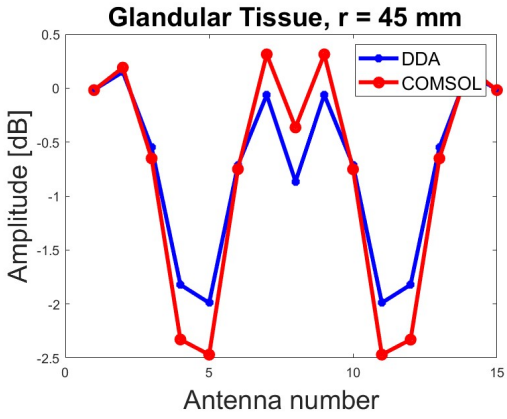

(f) S14

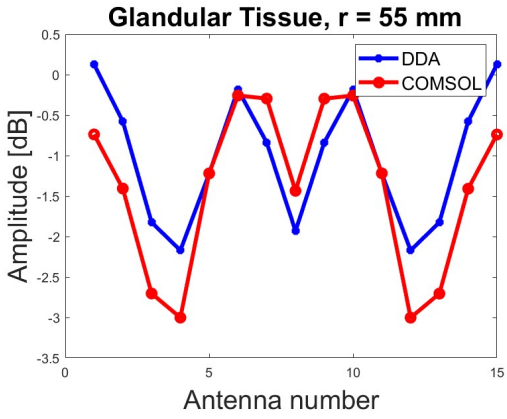

(g) S15

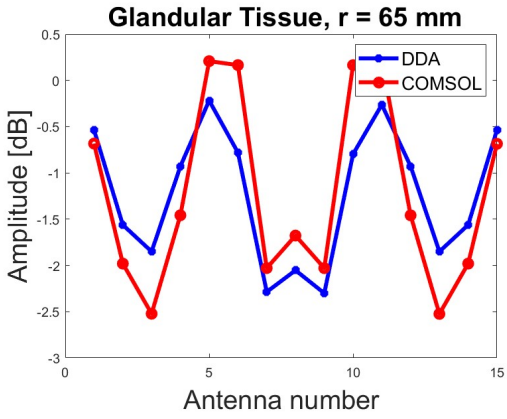

(h) S16

Figure 4.5: Calibrated amplitude for the size evaluation of a fibroglandular object.

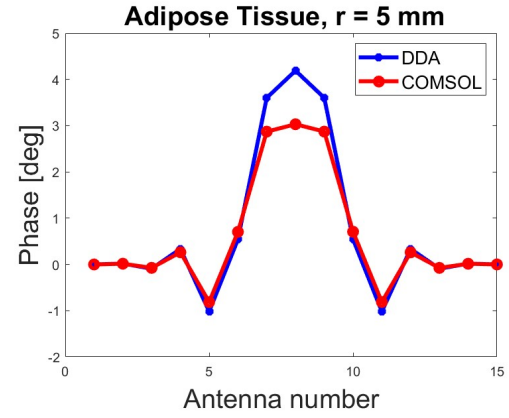

(a) S1

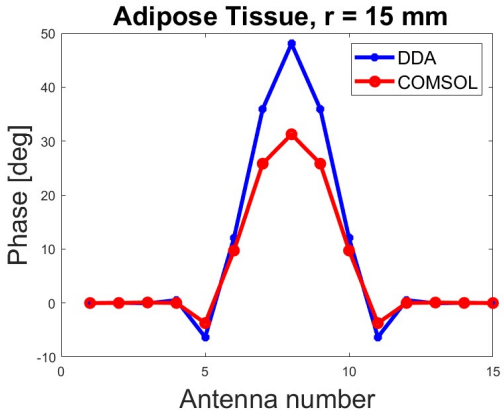

(b) S2

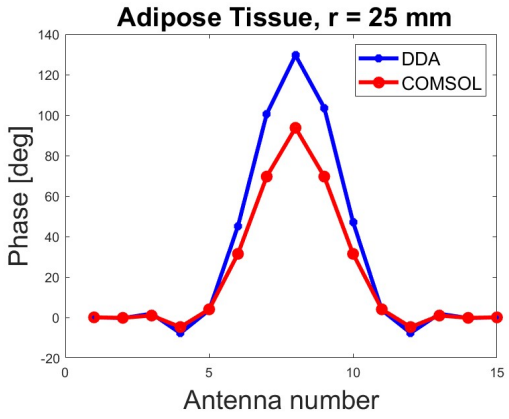

(c) S3

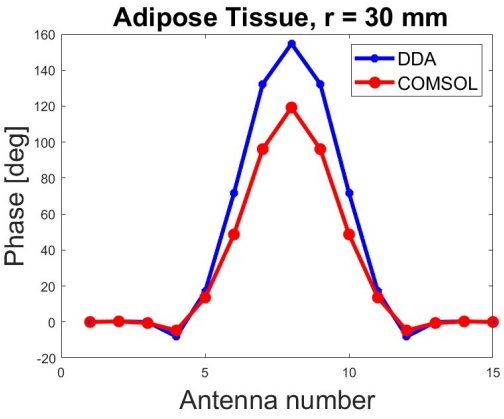

(d) S4

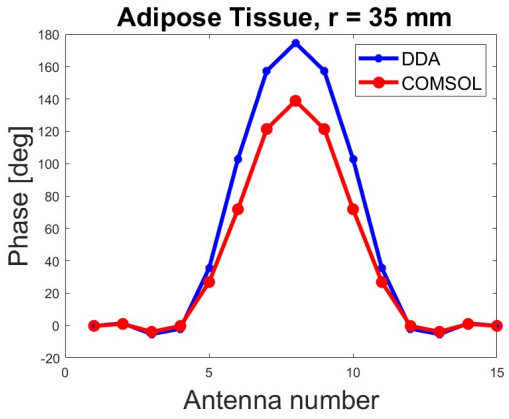

(e) S5

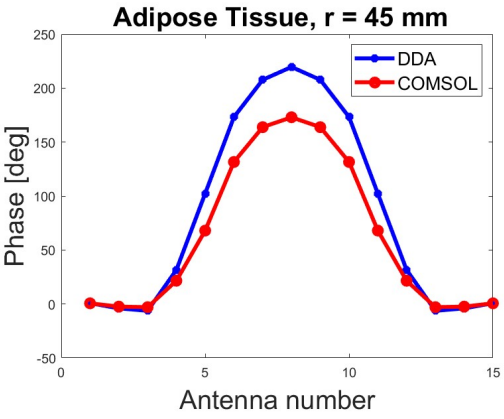

(f) S6

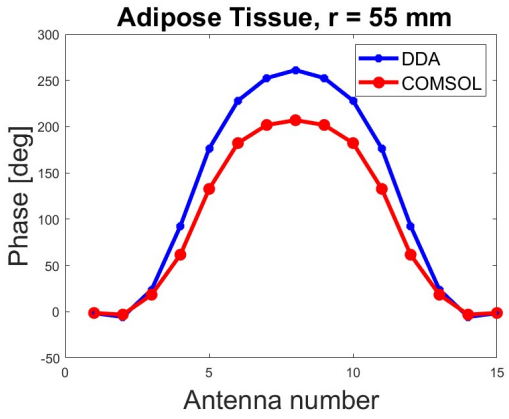

(g) S7

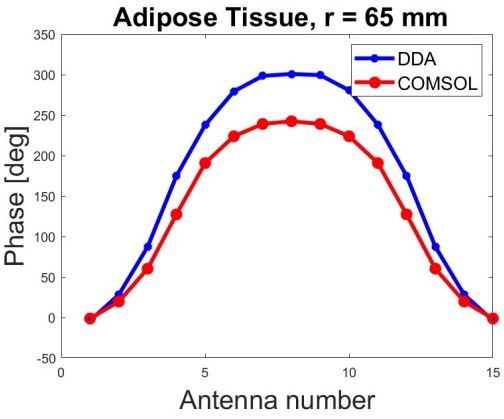

(h) S8

Figure 4.6: Calibrated phase for the size evaluation of an adipose object.

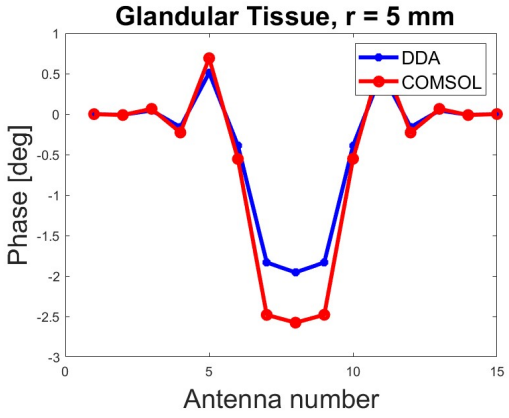

(a) S9

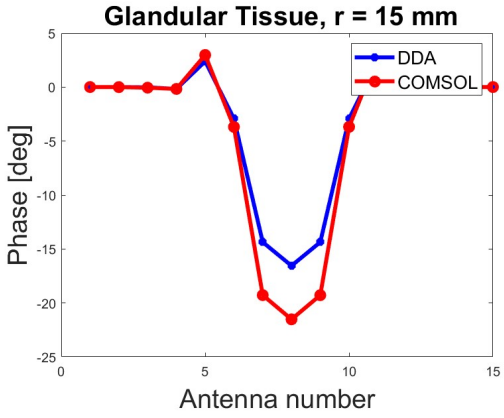

(b) S10

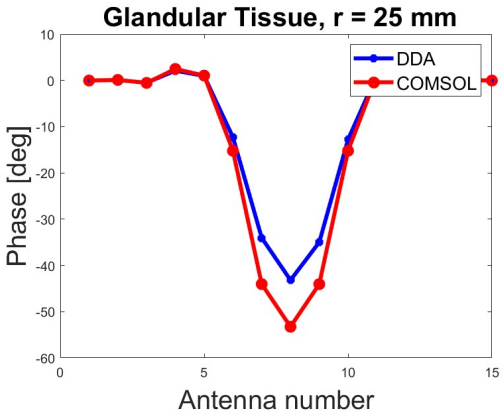

(c) S11

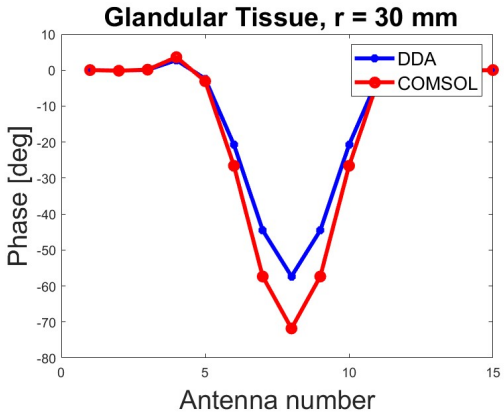

(d) S12

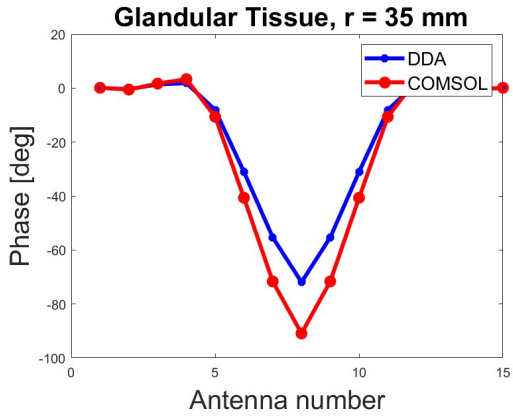

(e) S13

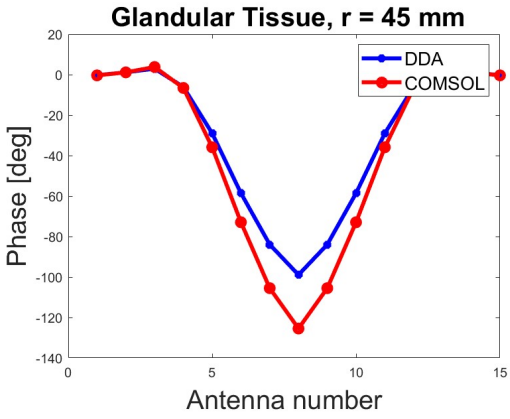

(f) S14

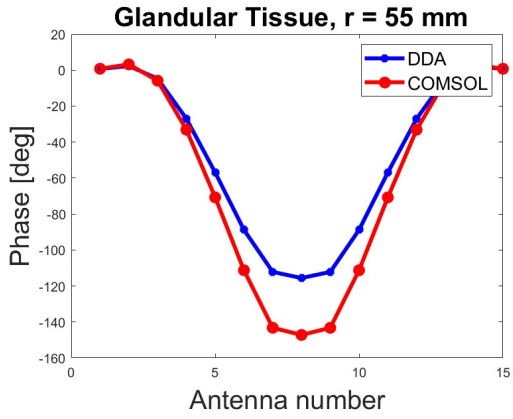

(g) S15

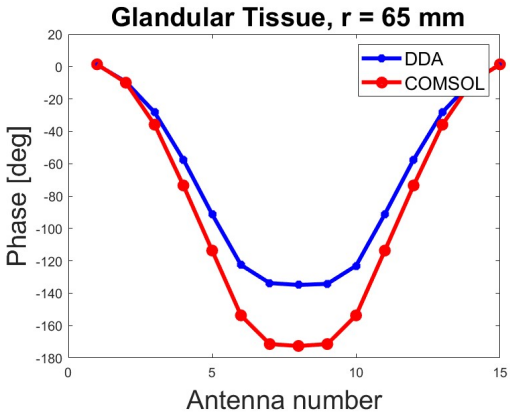

(h) S16

Figure 4.7: Calibrated phase for the size evaluation of a fibroglandular object.

The results from the size evaluation including the FDTD forward solution to generate the E-field can be seen in Figures 4.8-4.11, simulation IDs S2, S7, S10 and S15. The FDTD solutions are close to identical to the COMSOL solution, both regarding amplitude and phase for both tissue types and sizes. This result was imperative for later using FDTD to reconstruct the MRIs.

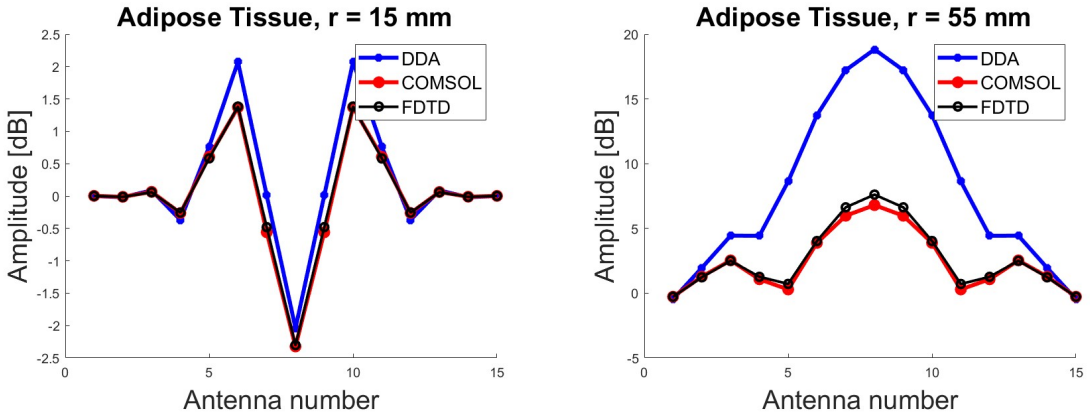

(a) S2 **(b)** S7

Figure 4.8: Calibrated amplitude for the size evaluation of an adipose object comparing DDA, COMSOL and FDTD.

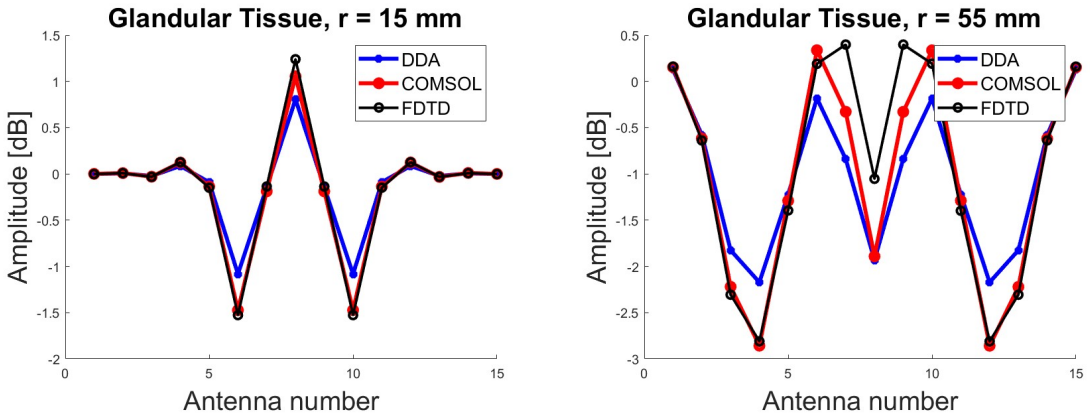

(a) S10 **(b)** S15

Figure 4.9: Calibrated amplitude for the size evaluation of a fibroglandular object comparing DDA, COMSOL and FDTD.

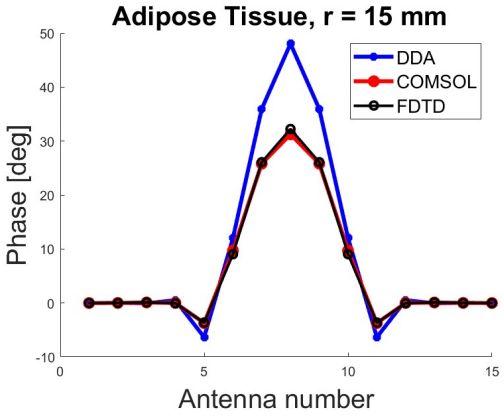

(a) S2

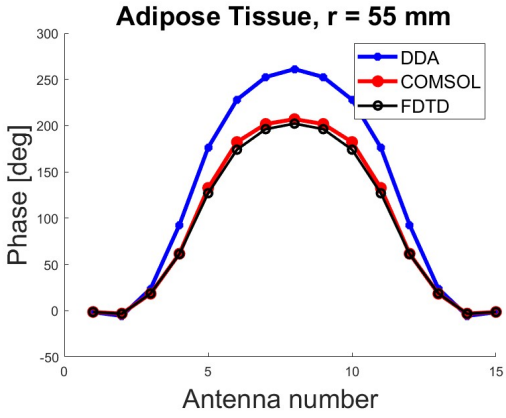

(b) S7

Figure 4.10: Calibrated phase for the size evaluation of an adipose object comparing DDA, COMSOL and FDTD.

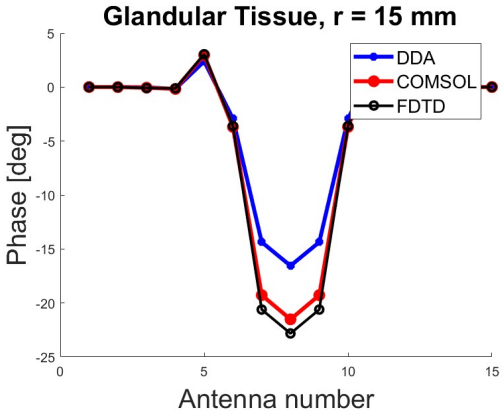

(a) S10

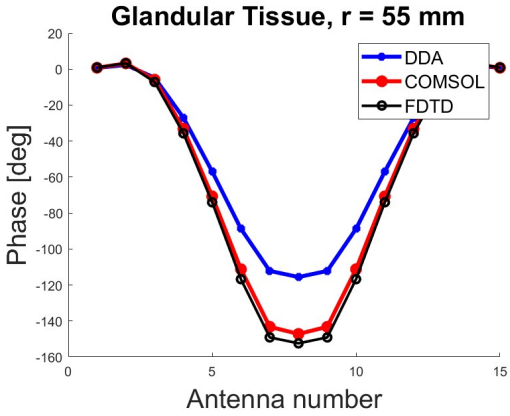

(b) S15

Figure 4.11: Calibrated phase for the size evaluation of a fibroglandular object comparing DDA, COMSOL and FDTD.

4.3 Dielectric Properties Evaluation

The results from the dielectric evaluation can be seen in Figures 4.12-4.17. The heatmaps in Figures 4.12-4.15 show clearly how the RMS increases when the dielectric properties deviates more from the background, more so for lower values than higher.

Figures 4.16a-4.16d shows the calibrated amplitude, corresponding to simulation IDs Di1-Di4 where the permittivity is altered, and Figures 4.16e-4.16h shows the calibrated amplitude, corresponding to simulation IDs Di5-Di8 where the conductivity is altered. Figure 4.17 shows the calibrated phases for the respective simulations. In accordance with previous results, an object with higher dielectric properties than the background gives a better correspondence between the two forward solution methods, this is especially apparent for the conductivity.

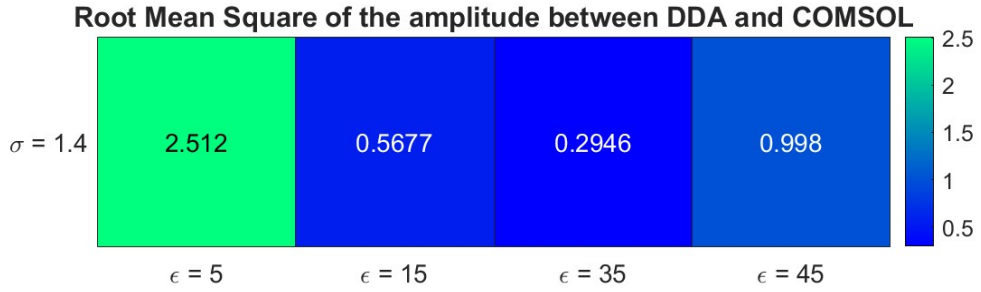

Figure 4.12: Heatmap of the amplitude RMS for the dielectric properties evaluation of the permittivity.

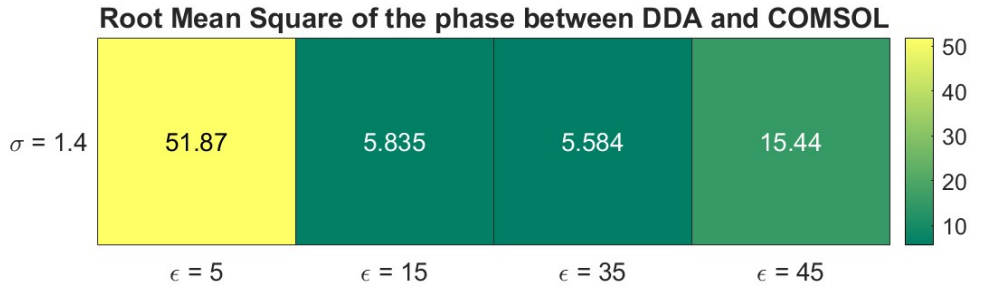

Figure 4.13: Heatmap of the phase RMS for the dielectric properties evaluation of the permittivity.

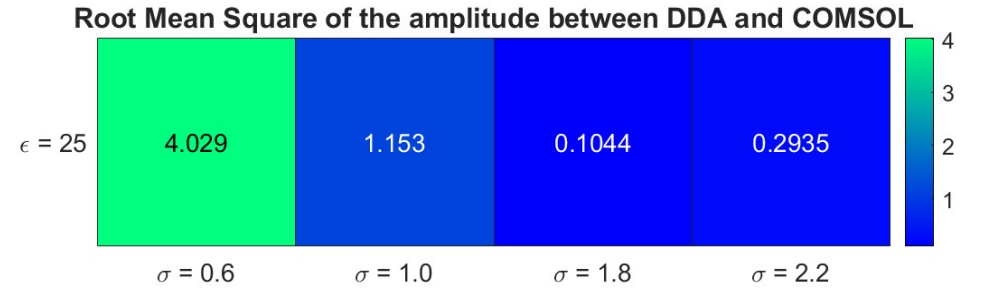

Figure 4.14: Heatmap of the amplitude RMS for the dielectric properties evaluation of the conductivity.

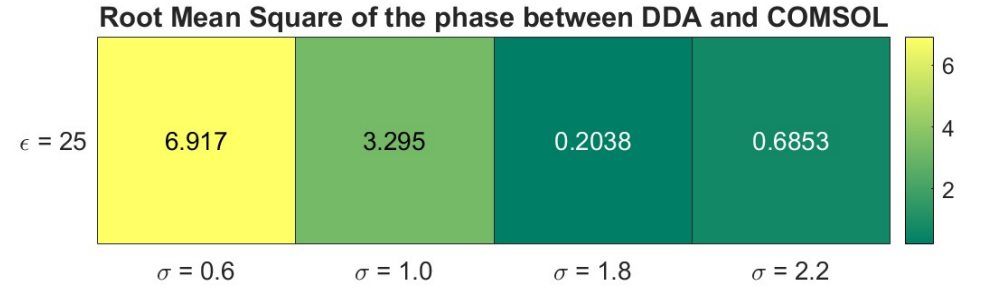

Figure 4.15: Heatmap of the phase RMS for the dielectric properties evaluation of the conductivity.

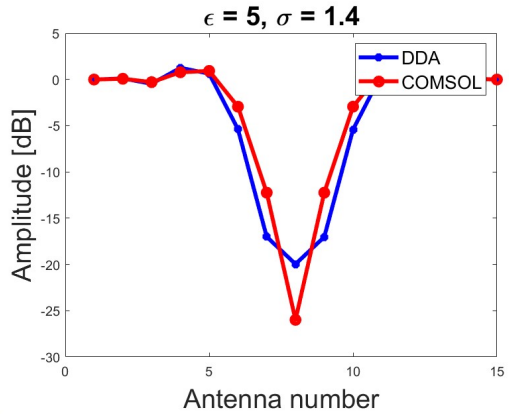

(a) Di1

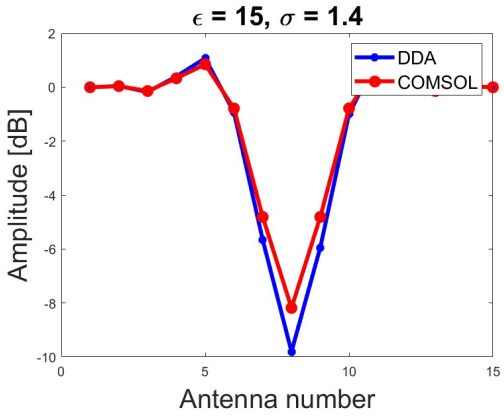

(b) Di2

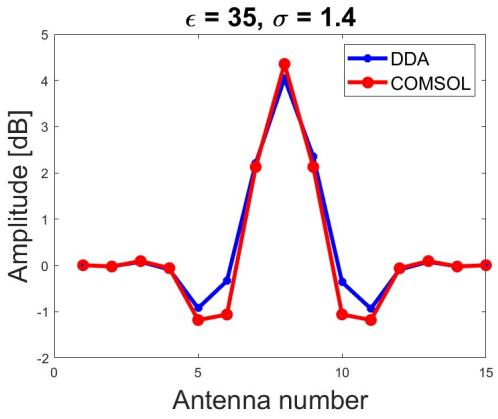

(c) Di3

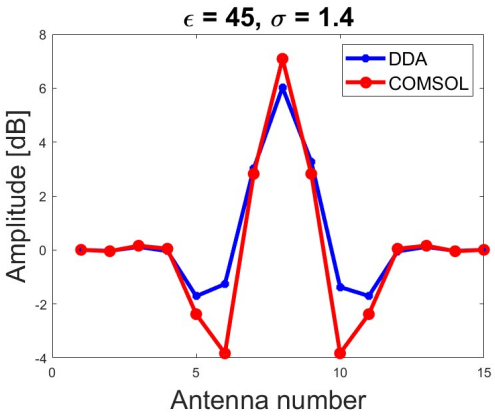

(d) Di4

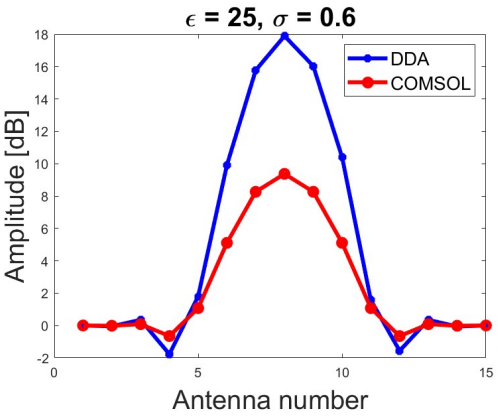

(e) Di5

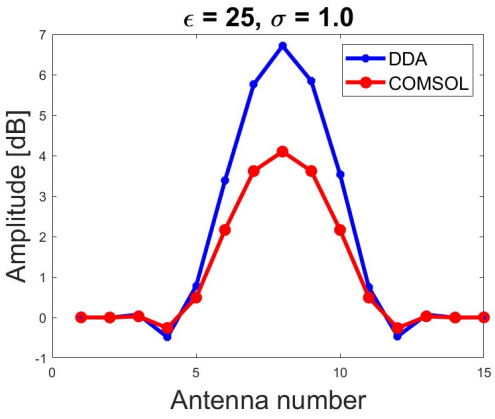

(f) Di6

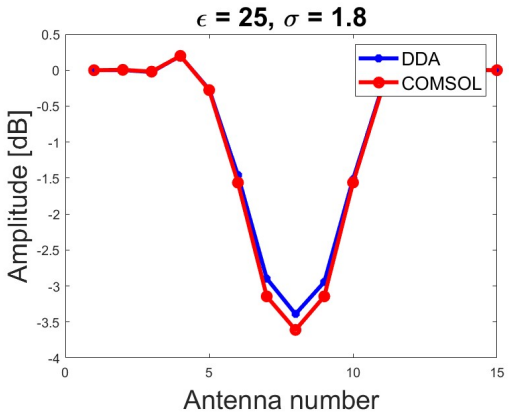

(g) Di7

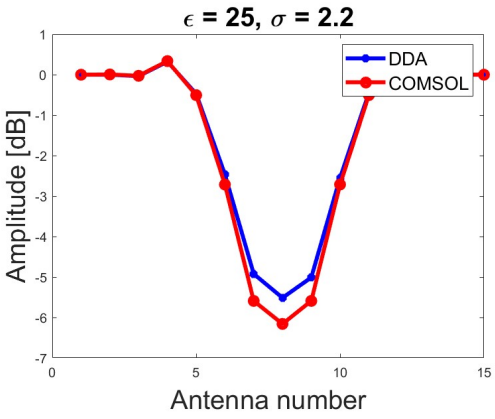

(h) Di8

Figure 4.16: Calibrated amplitude and phase for the dielectric properties evaluation of the permittivity.

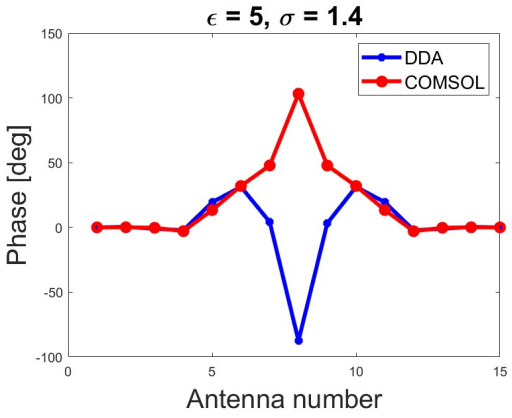

(a) Di1

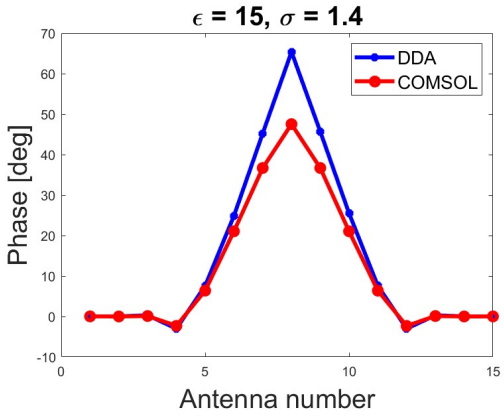

(b) Di2

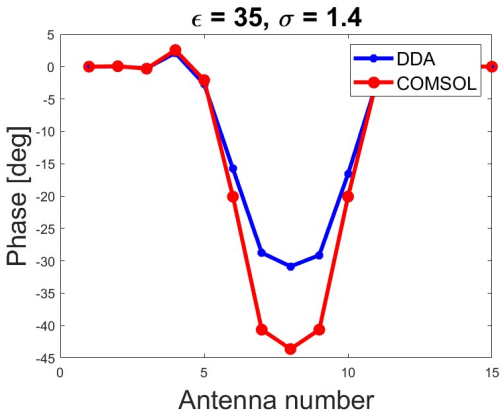

(c) Di3

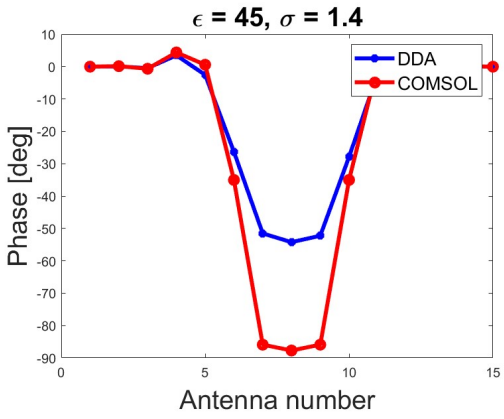

(d) Di4

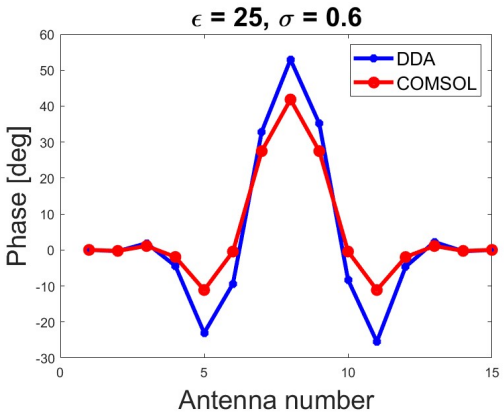

(e) Di5

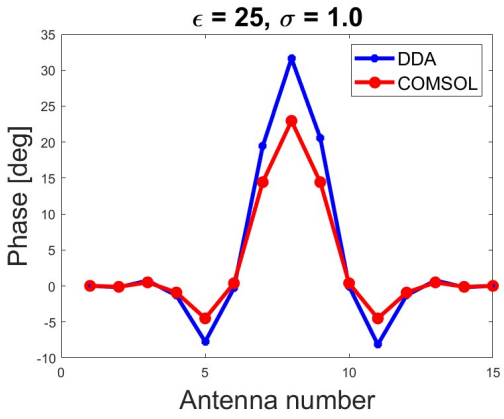

(f) Di6

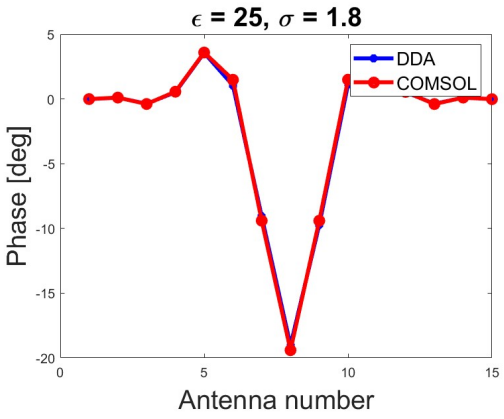

(g) Di7

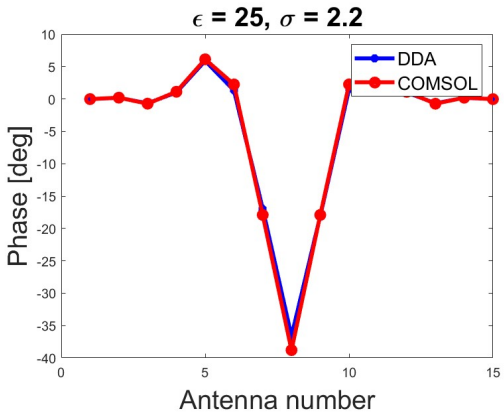

(h) Di8

Figure 4.17: Calibrated amplitude and phase for the dielectric properties evaluation of the conductivity.

A note from Figures 4.16 and 4.17 is that dielectric properties that are higher than the background consistently gives convex curves while lower dielectric properties gives concave curves, except in one case. The phase in the DDA solution for a very low permittivity (Fig. 4.17a) gives a deviating result where the peak is pointing downwards instead of up. For this reason the phase simulation data (i.e. the phase before the background is subtracted) is included and compared to that of a homogeneous background, see Figure 4.18. The object with very low permittivity (Fig. 4.18b) has a very sharp edge at the minimum, a discontinuity, which is normally not the case. When inspecting the phase propagation through the image domain in Figure 4.19, the appearance resembles a double-slit.

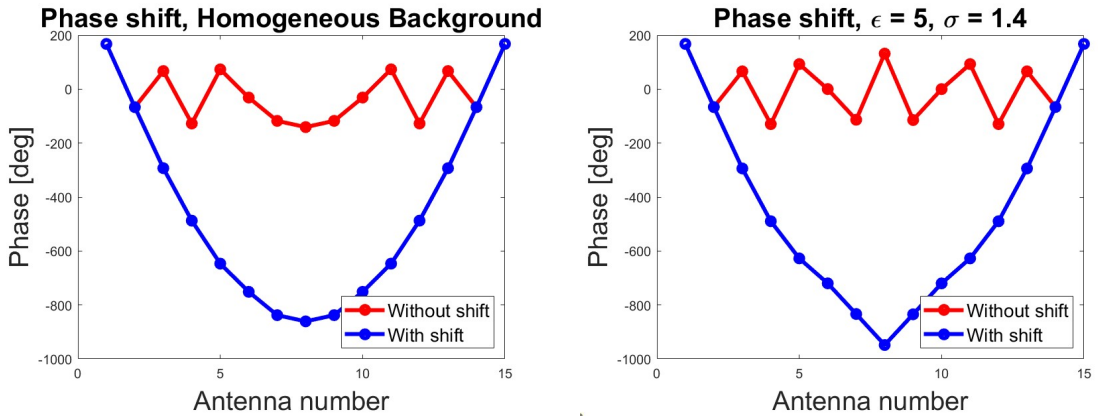

(a) Background **(b)** Di1

Figure 4.18: Comparison of the shape of the phase curve for homogeneous background and simulation Di1.

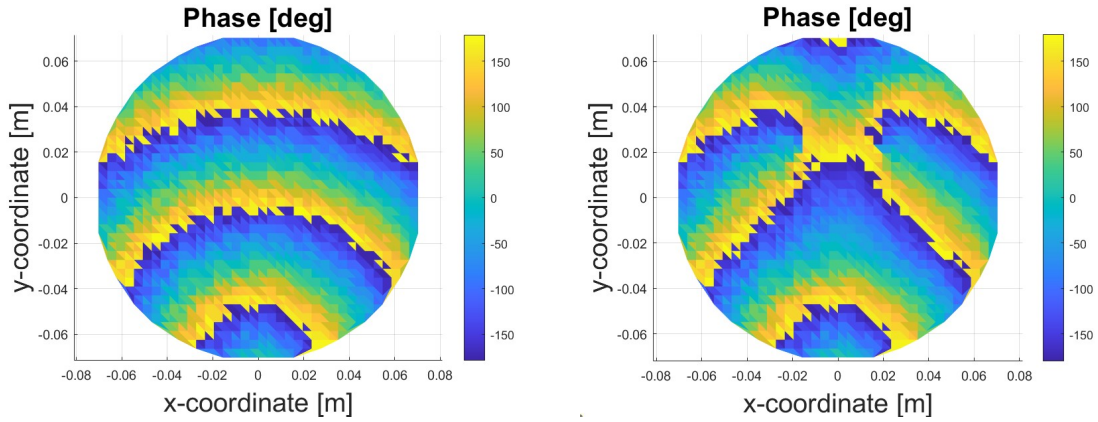

(a) Background **(b)** Di1

Figure 4.19: Phase propagation for homogeneous background and simulation Di1.

4.4 Concentric Circles Evaluation

The results from the concentric circle evaluation can be seen in Figures 4.20-4.24. The fifteen different combinations of fibroglandular circles surrounded by adipose tissue are summarized in the heatmaps in Figures 4.20-4.21, showing the amplitude RMS and phase RMS. The amplitude RMS increases with the size of the adipose circle and decreases with the increased size of the fibroglandular object. The smallest amplitude RMS was found for simulation CC5 (r_{outer} = 30 mm, r_{inner} = 40) and the largest was for to CC11 (r_{outer} = 10 mm, r_{inner} = 60 mm). The phase RMS generally increased with both the outer and inner circle radius, but that was not always the case, e.g. simulation CC2 (r_{outer} = 15 mm, r_{inner} = 40 mm). Calibrated amplitude and phase plot are only provided for these two amplitude RMS extreme cases, see Figures 4.22 and 4.23. When comparing these to the previous results, this more complex geometry causes greater differences in both shape and size for the plots. Additionally, phase propagation plots are provided, see Figure 4.24. These show a clear difference in propagation and phase shifts.

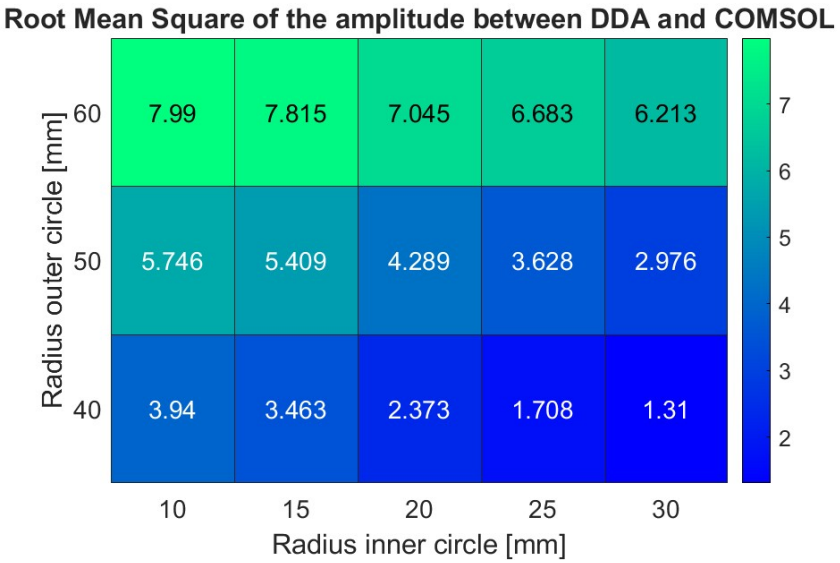

Figure 4.20: Heatmap of the amplitude RMS for the concentric circles evaluation.

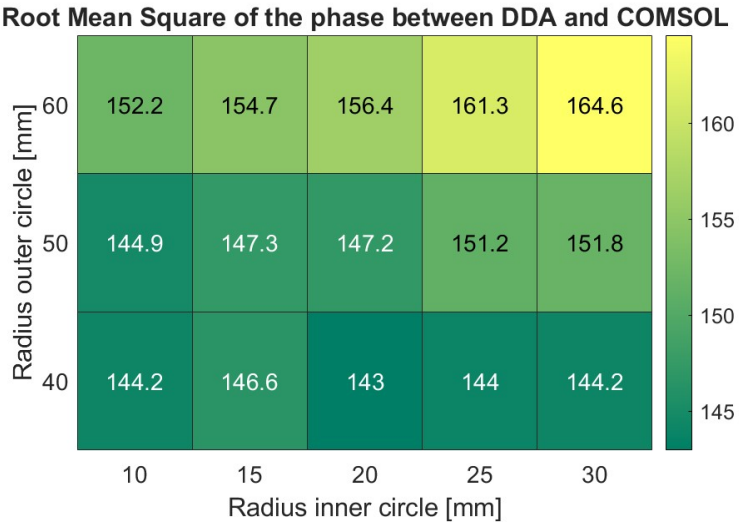

Figure 4.21: Heatmap of the phase RMS for the concentric circles evaluation.

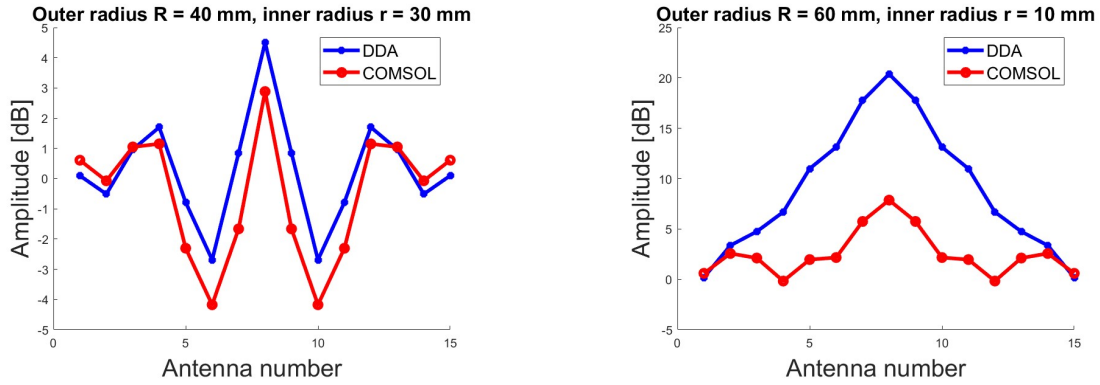

(a) CC5 (b) CC11

Figure 4.22: Calibrated amplitude for the concentric circles evaluation for simulations CC5 and CC11.

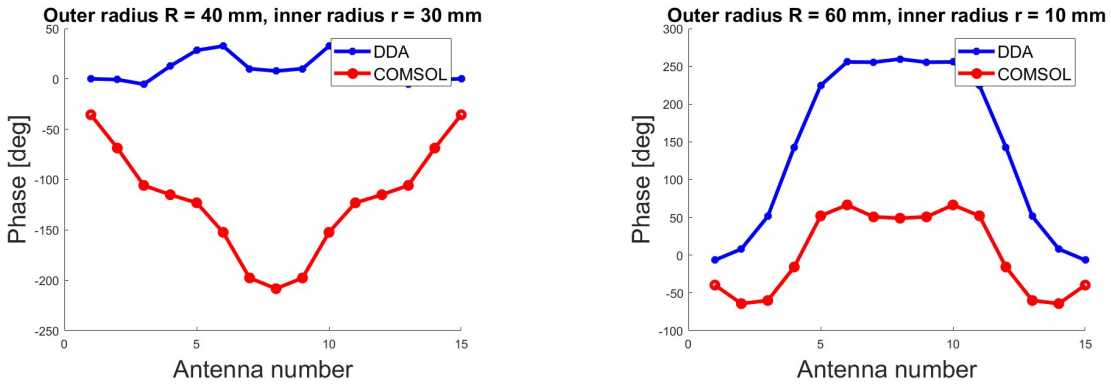

(a) CC5 (b) CC11

Figure 4.23: Calibrated phase for the concentric circles evaluation for simulations CC5 and CC11.

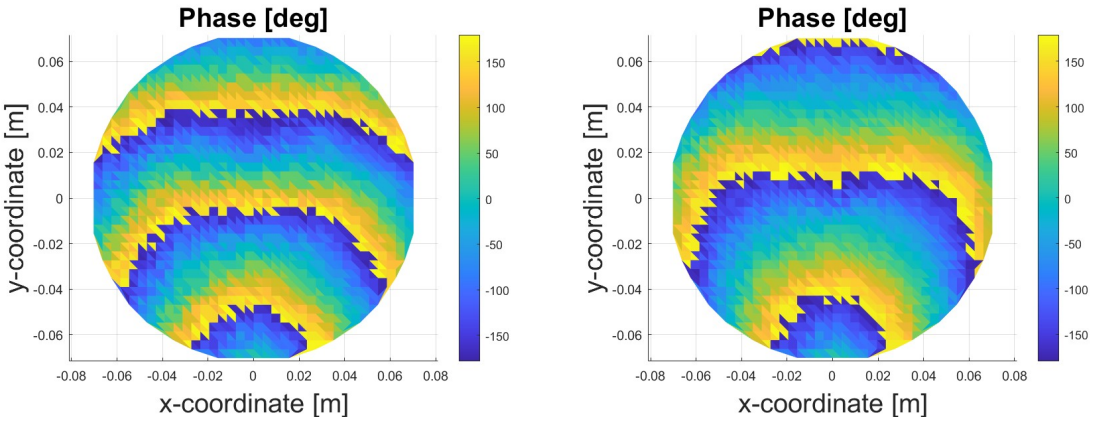

(a) CC5 (b) CC11

Figure 4.24: Phase propagation for the concentric circles evaluation for simulations CC5 and CC11.

4.5 Reconstructions

The generated reconstructions are presented in this section. Both permittivity and conductivity is reconstructed and compared to the original dielectric distributions. Starting with the four simulations of adipose and fibroglandular objects of sizes $r = 1.5$ cm and $r = 5.5$ cm respectively, where DDA, COMSOL and FDTD have been used to generate the forward solutions. After that a more complex geometry is tried using the MRI phantom for the two different cases.

4.5.1 Simulations

The reconstructions of simulations S2, S7, S10 and S15 can be seen in Figures 4.25-4.28. The reconstructions of small objects (Fig. 4.25-4.26) worked fairly well for 20 iterations. The shape is correct, though a bit blurry, but the objects did not reach their target dielectric values. The DDA solution generated a reconstruction slightly closer to the target values for the adipose object (Fig. 4.25) but the opposite was true for the fibroglandular object (Fig. 4.26).

In the reconstruction of large objects (Fig. 4.27-4.28) the reconstruction algorithm ended prematurely. The convergence criteria broke the reconstruction when an iteration increased the convergence instead of decreasing it. Notwithstanding, the shape of the large objects is quite clear in the adipose case that ran for 9-14 iteration, especially for the conductivity DDA case (Fig. 4.27f). There are also quite a lot of reflections at the antenna positions present, which was not the case for the smaller objects. In the fibroglandular case it is hard to make out anything more than a slightly lighter blue big circle and the antenna positions.

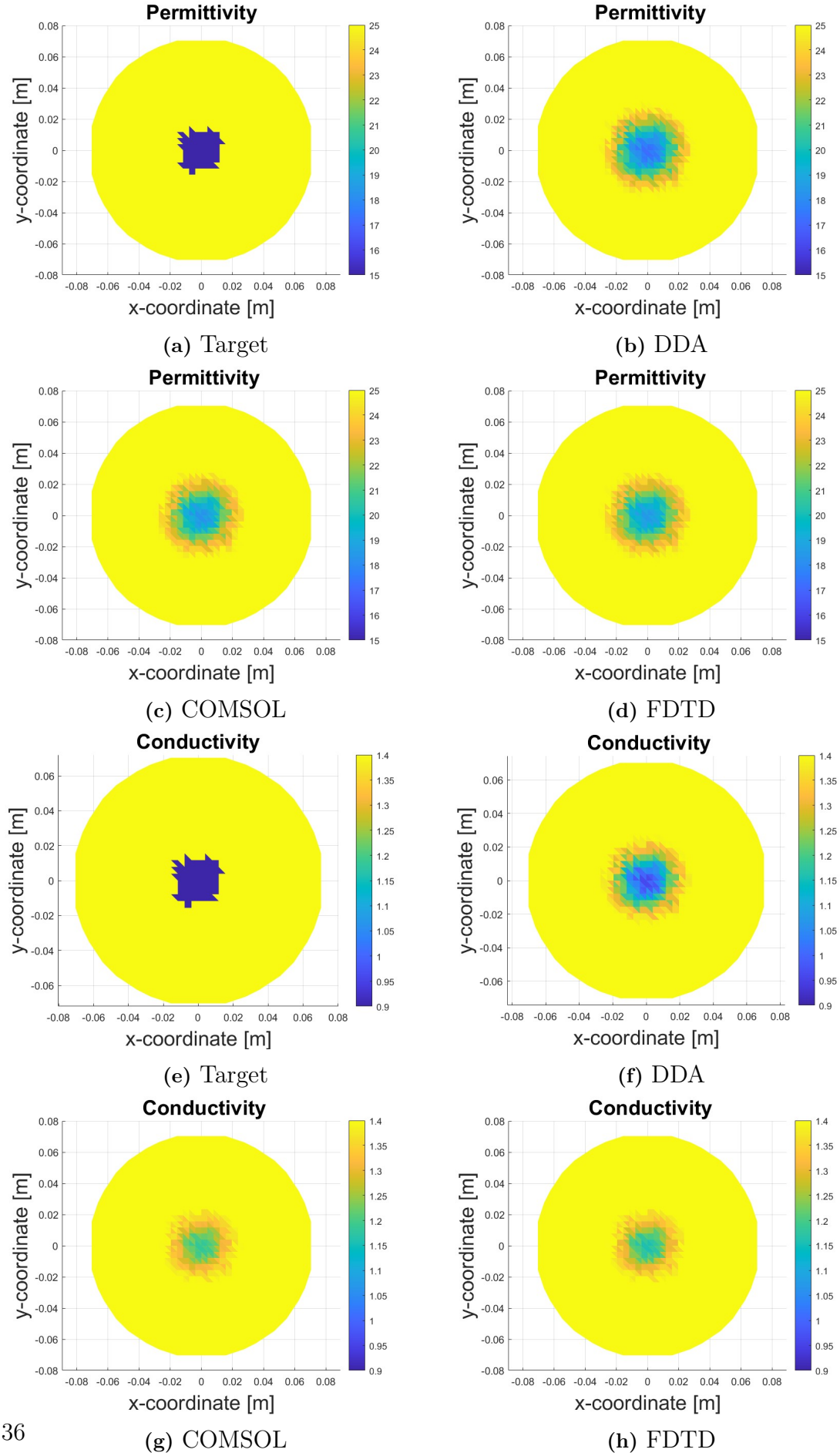

(a) Target (b) DDA

(c) COMSOL (d) FDTD

(e) Target (f) DDA

(g) COMSOL (h) FDTD

Figure 4.25: Reconstruction of an adipose object with $r = 15$ mm.

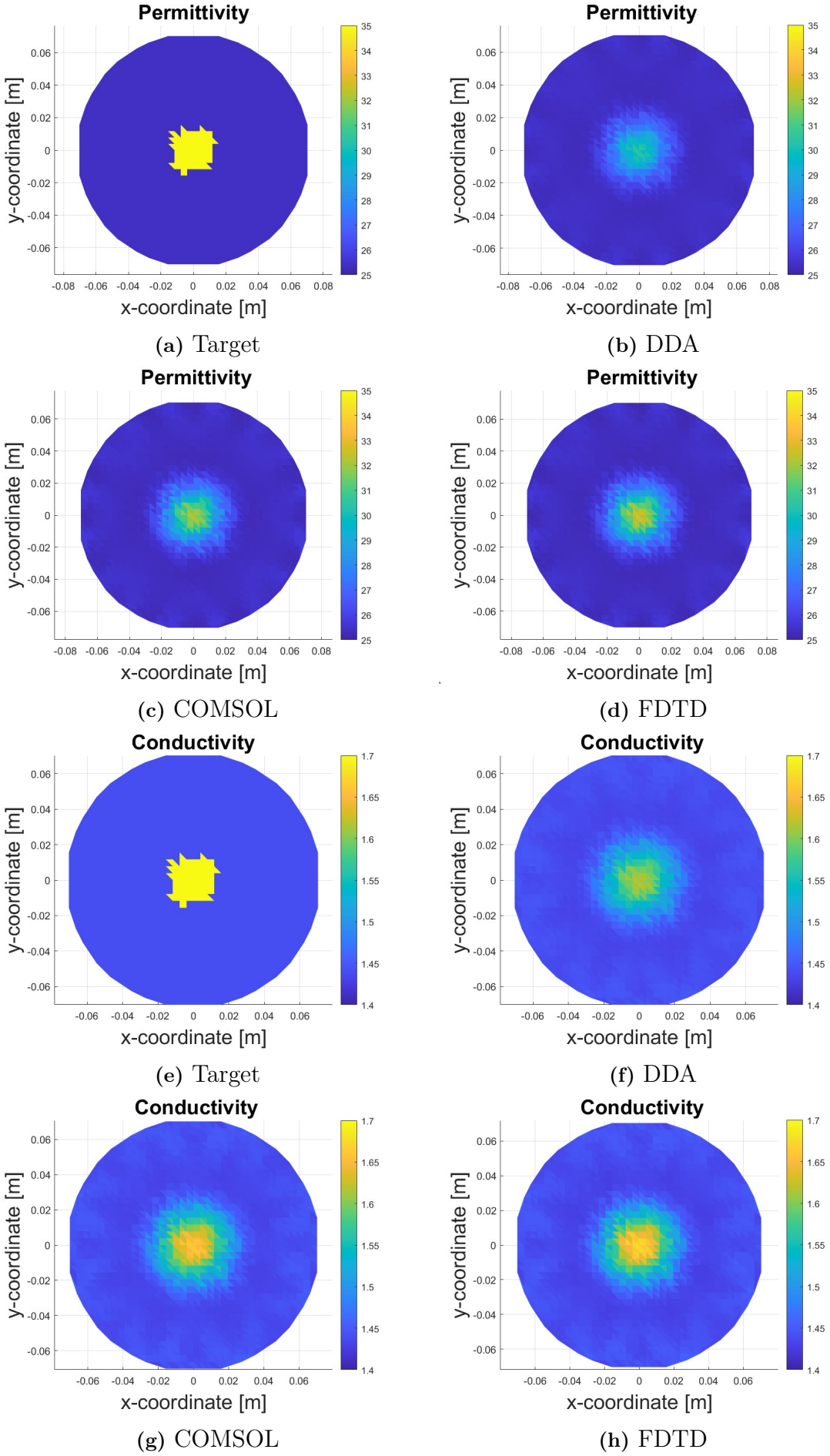

(a) Target (b) DDA

(c) COMSOL (d) FDTD

(e) Target (f) DDA

(g) COMSOL (h) FDTD

Figure 4.26: Reconstruction of a fibroglandular object with $r = 15$ mm.

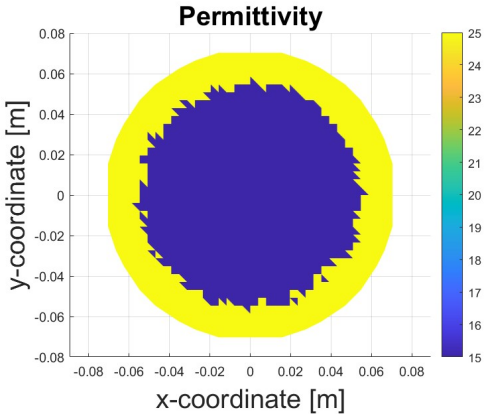

(a) Target

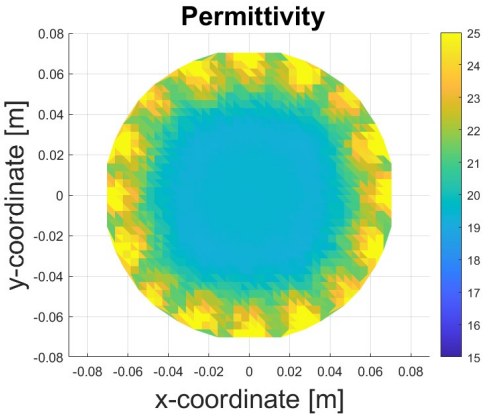

(b) DDA, broke after 9 iterations

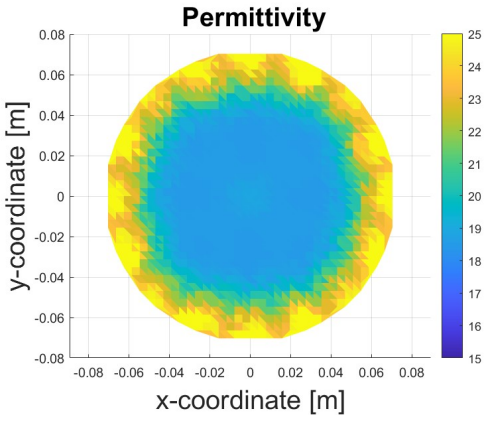

(c) COMSOL, broke after 14 iterations

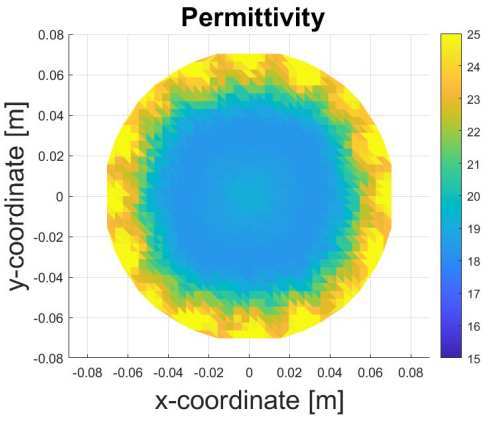

(d) FDTD, broke after 14 iterations

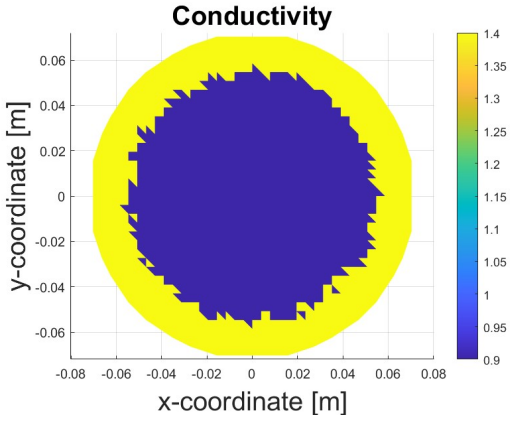

(e) Target

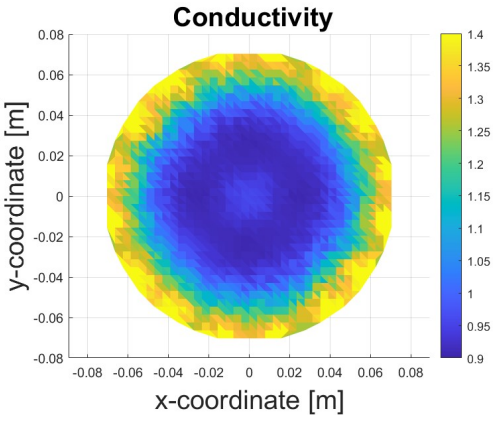

(f) DDA, broke after 9 iterations

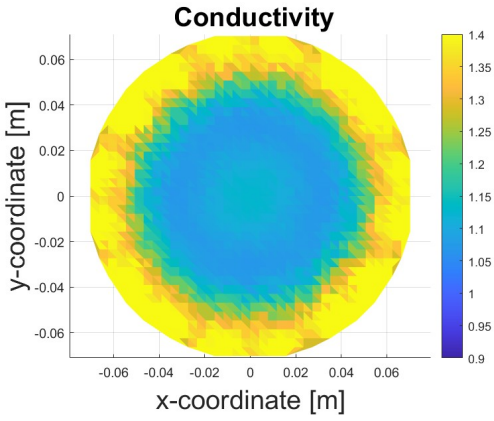

(g) COMSOL, broke after 14 iterations

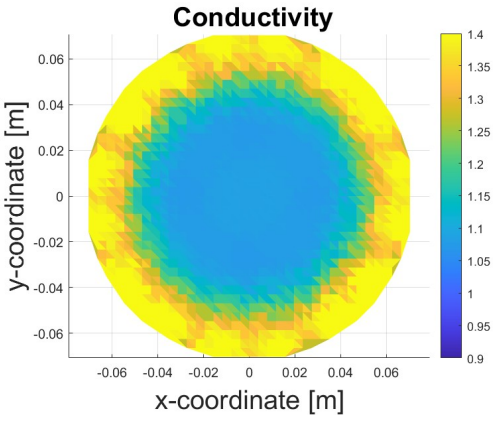

(h) FDTD, broke after 14 iterations

Figure 4.27: Reconstruction of an adipose object with $r = 55$ mm.

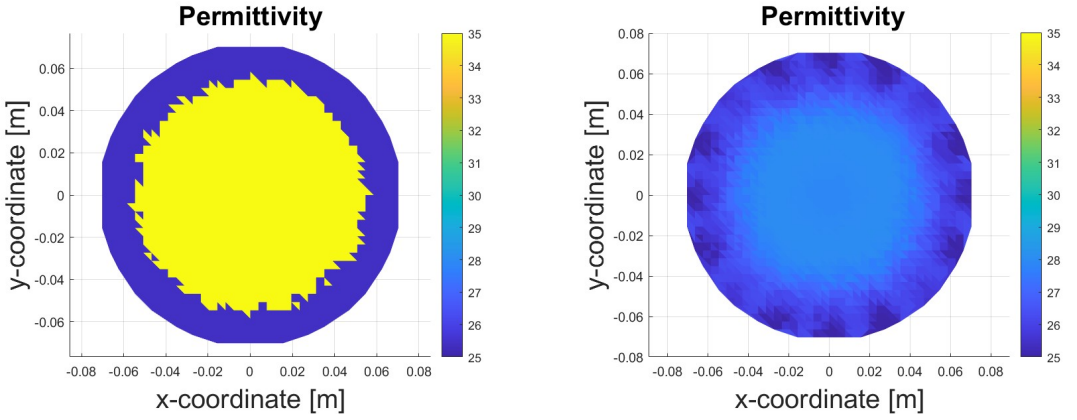

(a) Target

(b) DDA, broke after 6 iterations

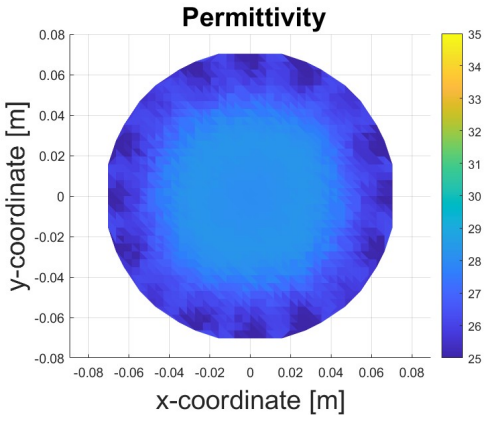

(c) COMSOL, broke after 5 iterations

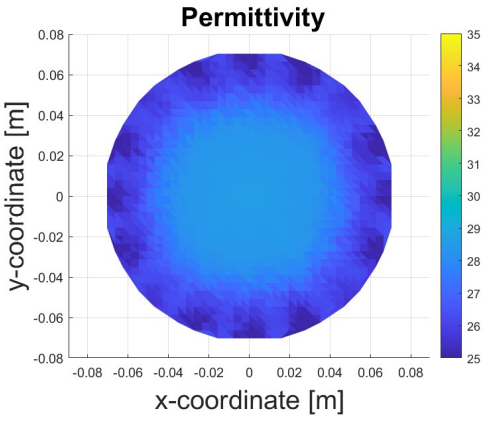

(d) FDTD, broke after 5 iterations

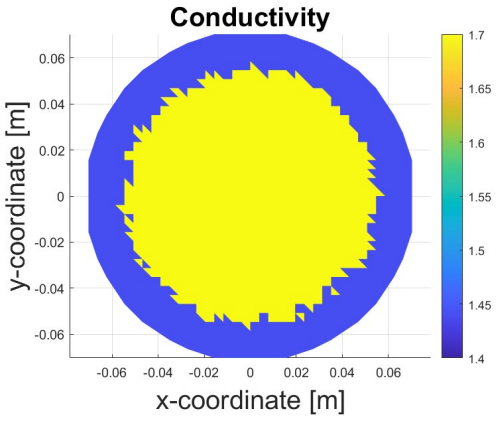

(e) Target

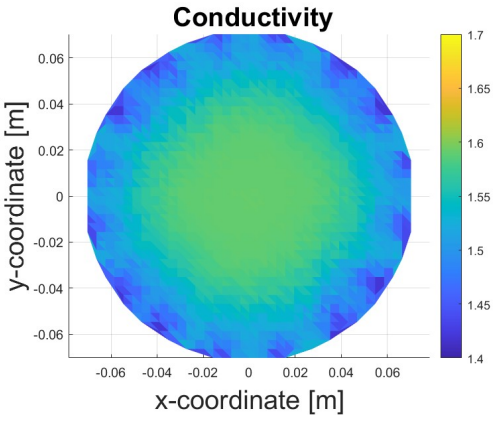

(f) DDA, broke after 6 iterations

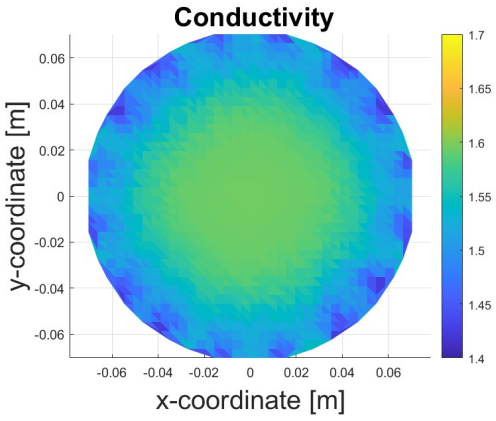

(g) COMSOL, broke after 5 iterations

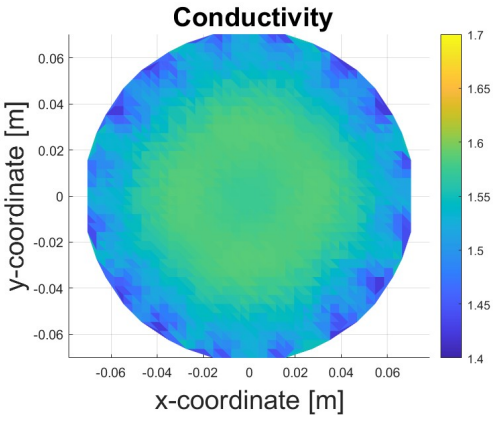

(h) FDTD, broke after 5 iterations

Figure 4.28: Reconstruction of a fibroglandular object with $r = 55$ mm.

Lastly, it could be seen that increasing the number of iterations generated a better result, see Figures 4.29-4.30. 20 iterations takes around 100 s, while 50 iterations takes just above 250 s.

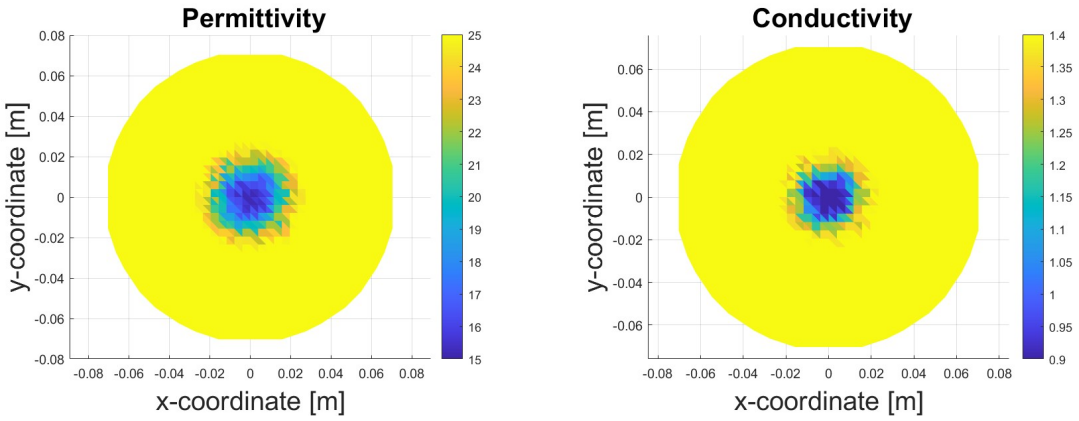

(a) DDA 50 iterations, ϵ **(b)** DDA 50 iterations, σ

Figure 4.29: Reconstruction of an adipose object with $r = 15$ mm, using 50 iterations.

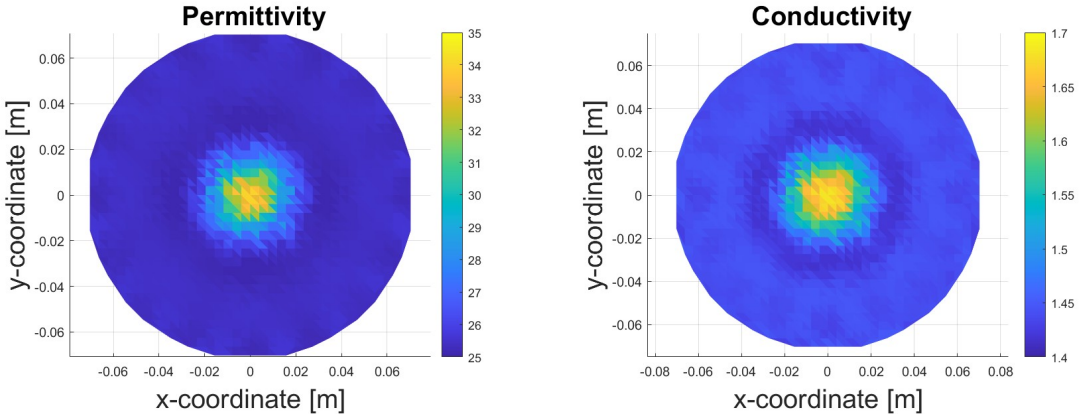

(a) DDA 50 iterations, ϵ **(b)** DDA 50 iterations, σ

Figure 4.30: Reconstruction of a fibroglandular object with $r = 15$ mm, using 50 iterations.

4.5.2 MRI Phantoms

The reconstruction of the MRI phantoms can be seen in Figures 4.31-4.32. Neither of the reconstructions surpassed four iterations. The reconstruction using a 3.9 mm grid and the DDA forward solution (Fig. 4.31) broke after only three iterations and the reconstruction is very hard to interpret. The reconstruction using a 1 mm grid and the FDTD forward solution (Fig. 4.32) passed four iterations before it broke prematurely, and the results are almost equally interpretable.

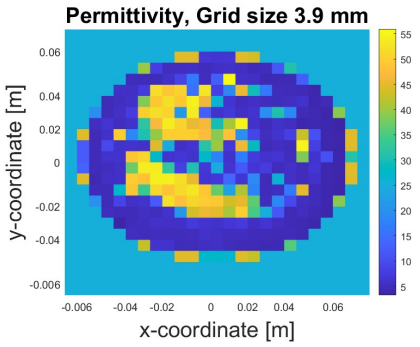

(a) Target

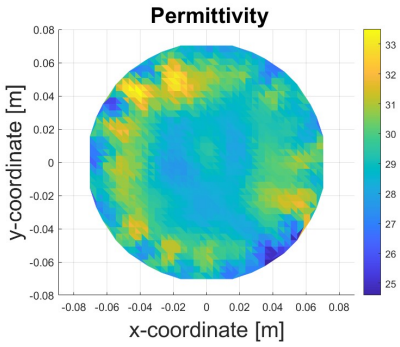

(b) DDA, broke after 3 iterations

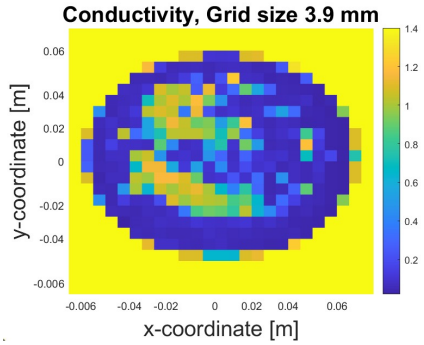

(c) Target

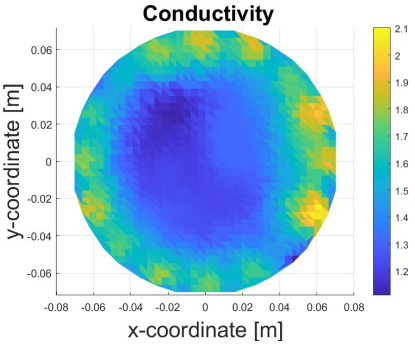

(d) DDA, broke after 3 iterations

Figure 4.31: Reconstruction of the MRI phantom, grid size 3.9 mm, using DDA.

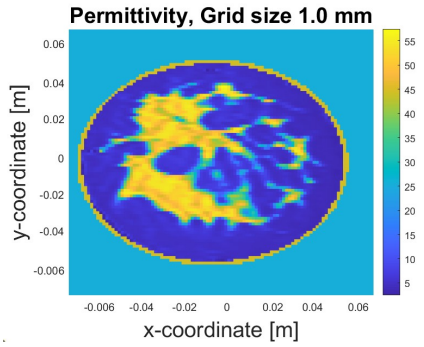

(a) Target

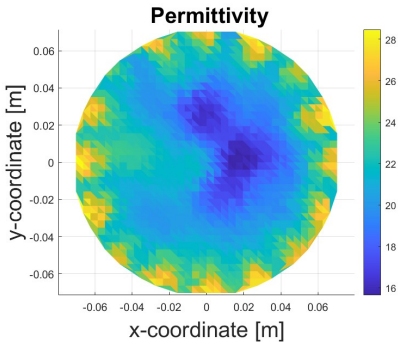

(b) FDTD, broke after 4 iterations

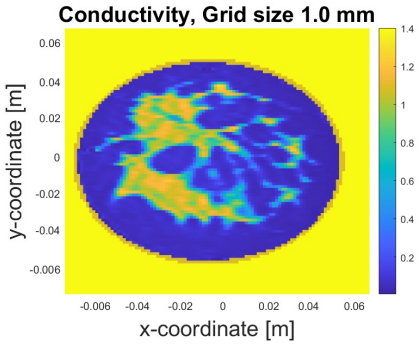

(c) Target

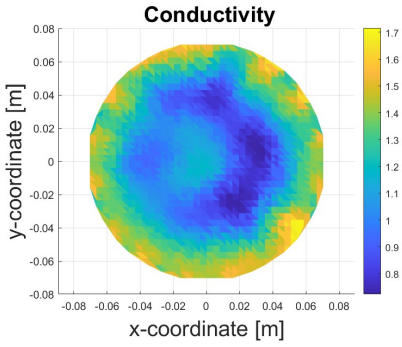

(d) FDTD, broke after 4 iterations

Figure 4.32: Reconstruction of the MRI phantom, grid size 1 mm, using FDTD.

5
Discussion

In this chapter the results from the heatmaps, calibrated amplitude and phase plots as well as the performed reconstructions are discussed. Starting in the beginning with the convergence study, and ending with some suggestions on future work that could not be performed within the scope of this thesis.

5.1 Convergence Study

The convergence study where a few different grid and mesh sizes were tried, showed that a spacing of 3.906 mm is fine enough and the results following from that point on can be considered reliable. In the DDA algorithm, a grid size of 1 mm is too small, causing computational errors because the matrices gets too large. 2 mm initially works, the code computes but a single run of the forward solution takes close to 30 min. If this smaller grid were to be used the computational time for a reconstruction would go back up to 10 h when using 20 iterations, which fully counteracts the purpose of the fast DDA algorithm. The grid size is therefore considered well balanced and the results reliable, even though a finer grid would off course better capture the geometry and dielectric changes in more complex and life-like simulations.

5.2 Size Evaluation

The size evaluation where the circle radius was varied between $r = 0.5 - 6.5$ cm showed a clear direct dependence between an object's size and the RMS difference in both calibrated amplitude and calibrated phase (Fig. 4.2-4.3). This was true for both higher and lower dielectric properties compared to the background. This was expected since a smaller object would reasonably have a smaller impact on the electromagnetic propagation through the image domain. For all smaller objects, $r < 3$ cm, the calibrated amplitude from the DDA and COMSOL forward solutions are very similar (Fig. 4.4a-4.4c, 4.5a-4.5c), which was the desirable outcome. For objects with higher dielectric properties than the background, this was true also for the larger sizes (Fig. 4.5). This leading up to the important note that for larger objects with lower dielectric properties, there is a large deviations between the forward solution methods (Fig. 4.4d-4.4h). This deviation was not expected nor is it fully understood as to why higher dielectric values generates good comparisons but large objects with lower values does not. It is however a very interesting and promising result. Objects with higher dielectric properties than the background are supposed to mimic fibroglandular tissue, which together with malignant tissue

typically have these higher values. In dense breasts where the glandular content is high, current screening methods have traditionally had more difficulty in separating dense tissue from possible tumours. So if the identification of small objects with high dielectric values are easily and correctly identified with microwave tomography, this technique will fill a gap in the current protocols for early detection.

When comparing the calibrated phase differences between the two solver methods, it is seen that objects with lower dielectric properties than the background (Fig. 4.6) have concave looking graphs, where the DDA solutions is always slightly above the COMSOL solution. For higher dielectric properties the opposite is true (Fig. 4.7). The graphs are then convex but the DDA solutions is still however slightly above the COMSOL solution. The RMS of the calibrated phases are somewhat high, but all phase graphs follow the same patterns when it comes to shape, peak orientation and scale, which makes the comparison easy to interpret and the dependency predictable.

When also including the FDTD forward solution (Fig. 4.8-4.11), it is clear that FDTD generates almost exactly the same results as the COMSOL simulations. That was the desired finding as well as an important one, put to practise at later stages in the thesis. This enables the reconstruction of more complex geometries, such as the MRI phantoms.

5.3 Dielectric Properties Evaluation

In accordance with the results from the size evaluation, the change in dielectric properties showed better resemblance between the different forward solution methods for values higher than the background, than it did for lowered tissue values. When altering the permittivity, all calibrated amplitude plots gave consistent and comparable solutions for both DDA and COMSOL (Fig. 4.16a-4.16d). The calibrated phase, however, works good for the smaller changes in permittivity (Fig. 4.17b-4.17c) but less so for larger differences (Fig. 4.17a, 4.17d). This is especially noticeable when the permittivity is reduced to $\epsilon = 5$ and the image domain phase propagation presents double-slit behaviour (Fig. 4.19b). This is in accordance with previous studies, where a very small permittivity have presented this behaviour and have therefore been hard to interpret.

A noticeable difference was in lowering and increasing the conductivity. A higher conductivity gave close to identical calibrated amplitude and phase plots for DDA and COMSOL (Fig. 4.16g-4.16h, 4.17g-4.17h), while lowered conductivity gave bigger differences, especially in the calibrated amplitude (Fig. 4.16e-4.17f).

The differences between the forward solutions increased with the increased difference in dielectric properties (Fig. 4.12-4.15), which was to be expected. The tried dielectric values were numerically evenly distributed, which might not have generated the most optimal nor most representative result. It might have been better for the comparison to use a percentage alteration in values compared to the background. Now, e.g. the increase in permittivity is almost 100 % while the decreases is a much as five times the original value, which is not comparable. However, it does clearly indicate the dependence that both of the dielectric properties have and it does include the range of values present in the MRI phantoms, so the findings are still of great importance.

5.4 Concentric Circles Evaluation

The results from the concentric circle simulations indicate that an over all smaller object works better than a larger object (Fig. 4.20-4.21). It also shows, in accordance with previous results, that a greater amount of high dielectric properties generates better results than when there is a high ratio of lower properties. This was very clear for the calibrated amplitude where the smallest RMS was for the smallest object consisting almost entirely of fibroglandular mimicking tissue, and the highest RMS was for the largest object consisting mostly of adipose mimicking tissue.

These simulations were a step towards a slightly more complex and realistic geometry, with object sizes and dielectric distributions close to actual breast anatomy. These results are therefore also more difficult to interpret. For the calibrated amplitude there is the described clear dependence, but the calibrated phase dependency is not as obvious. The deviations between the forward solutions are also greater for the concentric circles, than when compare with previous results in the size evaluation section, where homogeneous objects of the same sizes were used. The calibrated amplitude and phase plots start to have more peculiar appearances and deviations from one another (Fig. 4.22-4.23). Here the phase shift really comes into play, where it is clear that a whole more phase can propagate through an image domain with a small glandular object than with a larger adipose object (Fig. 4.24).

5.5 Reconstructions

The reconstruction algorithm works well for small objects with both lower and higher dielectric properties compared to the background (Fig. 4.25-4.26). The general shape is captured well but the dielectric distribution does not quite reach target values. In this thesis the difference between background and object properties was greater than in previous studies where the same fast DDA reconstruction algorithm has been used. This was in order to mimic real breast tissue distribution, so it is not too surprising that 20 iterations might not have been enough for these larger differences. It was therefore easily established that an increased number of iterations generated a dielectric distribution closer to the target (Fig. 4.29-4.30). Since each iteration takes roughly five seconds, it would be possible to increase the number of iterations, without increasing the computational time too much. It would still only take a few minutes and not tens of hours to reconstruct an image domain. This is especially motivated if it guarantees better dielectric distributions when there are large property differences between the breast tissues.

For larger objects that fill out almost the entire image domain (Fig. 4.27-4.28), the algorithm breaks before the 20 iterations have passed, due to the convergence criteria. When looking at the reconstructions, the large object is fairly easy to distinguish, but so are the reflections from the antennas, which should not be the case. This is somewhat in line with the previous simulation results. For larger objects, the DDA algorithm struggles to accurately capture the correct characteristics and dielectric distributions. Here the reconstructions of adipose mimicking objects lasted 9-14 iterations, compared to the glandular mimicking objects that only lasted 5-6

iteration. Again, it is clear that more iterations generates better results with both clearer geometries and with dielectric distributions closer to target. The adipose reconstructions have distinct lowered distributions in the middle of the image domain, making the object distinguishable. The fibroglandular reconstructions, however, break too early for any apparent shapes to be visible, and while the dielectric distributions are slightly increased in the middle of the image domain, no conclusions can be based on those reconstructions. The same arguments apply for the MRI phantom reconstructions (Fig. 4.31-4.32). The algorithm breaks after only 3-4 iterations. Notwithstanding, the reconstruction based on the FDTD forward solution generated E-field, ever so slightly captures darker and brighter regions, where expected. So, if able to work around the convergence criteria, it would be of highest interest to see how the distributions look after all 20 iterations. The FDTD solution using a finer grid generated better results than the DDA solution using a 3.9 mm grid. This indicating that the input E-field should be based on a grid size as fine as possible, to initially correctly capture the complex geometry and dielectric distributions.

The results from the reconstructions from the DDA, COMSOL and FDTD E-fields are all comparable. They generate similar reconstructs and it is the same cases that breaks beforehand and around the same number of iterations. This is an important finding since the comparability, and especially then the legitimacy of the DDA algorithm, can then be verified in the performed experimental simulations and reconstructions.

5.6 Ethical, Ecological and Social Aspects

The purpose of the microwave tomography systems that this thesis is based on, is that the technique will be used in a clinical application. That will have high ethical demands that needs to be taken into consideration and evaluated. However, in this thesis no clinical measurements were made, no patients were involved and no personal data was gathered. All measurements are either simulations or from pre-existing physical measurements, requiring no extra ethical permits nor resources. The thesis does therefore not have any ecological impact either. When the technique is ready for a clinical application, that will lead to completely harmless and pain free breast cancer screening, with several positive social aspects including increased detection, increased survival rate and milder treatments.

5.7 Future Work Suggestions

The general size of the MRI breast phantoms provided by UWCEM is $r = 4.5 - 5.5$ cm, e.g. around the size where the calibrated adipose amplitude and phase started to deviate, as well as the size for which the reconstructions ended prematurely. Two paths are of interest here. The first is to keep the dielectric properties constant and decrease the object size when performing reconstructions. This in order to find how large objects the reconstruction algorithm can handle for the given properties. The second path is keeping this realistic size and instead change the dielectric properties to be closer to the background, both above and below the background values. This

to give a better understanding of how big the differences can actually be. In this thesis the dielectric properties of the background were never altered. That would also be a good start when looking into larger object and more complex geometries, such as the MRI phantoms, and why they ended the iterations prematurely. It is of interest to see if a change in the background properties, to better match the dominating tissue properties, generates a better result. It is also of interest to try more of the nine provided phantoms. In this thesis a class 3 phantom was used, with a high fibroglandular content. It would be of interest to use e.g. a class 1 phantom, which is almost entirely made up of adipose tissue, and especially if the background is adapted to that specific dielectric properties.

Since the reconstruction algorithm ended prematurely in several cases, it will be of importance to look into the convergence criteria. Adapting the background better might solve several issues, but the convergence criteria is still a big obstacle when as few as 3-4 iterations are being executed. Additionally, an automatic phase shift algorithm is needed. Right now they had to be performed manually, which is not sustainable in the long run.

The MRI voxel data was not found to be compatible with COMSOL, so a future recommendation is to prioritize resources to look into that. In this project the COMSOL solution was considered a foregone conclusion and therefore it is of high importance to be able to compare the COMSOL E-fields with those created using DDA. Since the FDTD forward solution gave calibrated amplitude and phase plots as well as reconstructions close to identical to COMSOL, this method was used for the MRI reconstruction in the meantime. That the compatibility solution was not found during this project does not mean it does not exist. Possibly finding it would enhance the evaluation of the DDA method in the reconstruction, especially for more complex geometries where the FDTD solution also slightly deviated from the COMSOL solution.

6
Conclusion

The DDA method works well as a forward solver for small objects, especially those with higher dielectric properties compared to the background. For larger objects the difference between the DDA, COMSOL and FDTD solutions becomes more prominent, with strongly deviating E-field amplitudes, especially for objects with lower dielectric properties compared to the background. The greater the difference is in the dielectric properties, the greater the difference becomes between the DDA, COMSOL and FDTD solutions. There is also a direct correlation between an object's size and the calibrated RMS difference between the DDA method and the other two methods.

When reconstructing small objects the general shape is correct, although with some blurry edges. The dielectric values does not however reach target values, but comes closer with an increased number of iterations. The input E-fields generated using the DDA method works better for low dielectric values, while the COMSOL and FDTD fields works better for high values. When reconstructing large objects the algorithm consistently encounters a terminating convergence criteria. The general shape can often be distinguished, at least in the case with lower dielectric properties. When reconstructing large objects there appear to be reflections at the antenna positions, which are not present when reconstructing small objects. The reconstruction of MRI phantoms proved too demanding within the scope of this thesis, due to the large size and big differences in tissue properties of the phantom, causing the algorithm to break prematurely.

Bibliography

[1] World Health Organization, "Breast Cancer." https://www.who.int/news-room/fact-sheets/detail/breast-cancer, 2021. Accessed on January 17, 2023.

[2] Global Cancer Observatory, "Cancer Today." https://gco.iarc.fr/, 2020. Accessed on May 22, 2023.

[3] Cancerfonden, "Mammografi." https://www.cancerfonden.se/om-cancer/undersokningar/mammografi, Year of publication, if available. Accessed on February 03, 2023.

[4] U. Fischer, F. Baum, and S. Luftner-Nagel, *Breast Cancer: Diagnostic Imaging and Therapeutic Guidance*. Thieme Medical Publishers, Incorporated, 2017.

[5] S. Hosseinzadegan, *A discrete dipole approximation forward solver for microwave breast imaging.* Technical report R / Department of Electrical Engineering, Group of Biomedical Electromagnetics, Chalmers University of Technology: 2019:3, Department of Electrical Engineering, Chalmers University of Technology, 2019.

[6] T. Grzegorczyk, P. Meaney, P. Kaufman, R. di Florio-Alexander, and K. Paulsen, "Fast 3-d tomographic microwave imaging for breast cancer detection.," *IEEE Transactions on Medical Imaging, Medical Imaging, IEEE Transactions on, IEEE Trans. Med. Imaging*, vol. 31, no. 8, pp. 1584 – 1592, 2012.

[7] T. Rydholm, *Experimental evaluation of a microwave tomography system for breast cancer detection.* Technical report. R: 2018:15, Department of Electrical Engineering, Chalmers University of Technology, 2018.

[8] Weerakkody Y, Niknejad M, Yap J, "Breast Imaging Reporting and Data System (BI-RADS)." https://radiopaedia.org/articles/breast-imaging-reporting-and-data-system-bi-rads?lang=us, 2022. Accessed on February 01, 2023.

[9] S. N. Sulaiman, M. H. Normazli, N. A. Harron, N. K. A. Karim, K. A. Ahmad, and Z. H. C. Soh, "A Convolutional Neural Network Model for Image Enhancement of Extremely Dense Breast Tissue in Digital Breast Tomosynthesis Images.," *2022 IEEE 12th International Conference on Control System, Computing and Engineering (ICCSCE), Control System, Computing and Engineering (ICCSCE), 2022 IEEE 12th International Conference on*, pp. 153 – 157, 2022.

[10] Campbell, Jean, "Dense Breasts and Breast Cancer Risk." https://www.verywellhealth.com/dense-breasts-430657, 2022. Accessed on May 19, 2023.

[11] U. Veronesi, A. Goldhirsch, P. Veronesi, O. D. Gentilini, and M. C. Leonardi, *Breast Cancer Innovations in Research and Management*. Springer Cham, 2017.

[12] U.S. Preventive Services Task Force, "A and B Recommendations." `https://www.uspreventiveservicestaskforce.org/uspstf/recommendation-topics/uspstf-a-and-b-recommendations#bcf`, 2022. Accessed on March 03, 2023.

[13] Canadian Task Force on Preventive Health Care, "Breast Cancer Update (2018)." `https://canadiantaskforce.ca/guidelines/published-guidelines/breast-cancer-update/`, 2018. Accessed on March 03, 2023.

[14] G. M. Newstead, *Breast MRI Interpretation: Text and Online Case Analysis for Screening and Diagnosis.* Thieme Medical Publishers, Incorporated, 2020.

[15] E. C. Lin and A. Alavi, *PET and PET/CT : A Clinical Guide.* Thieme Medical Publishers, Incorporated, 2019.

[16] J. L. Prince and J. M. Links, *Medical imaging signals and systems.* Pearson Prentice Hall, 2015.

[17] S. Hosseinzadegan, A. Fhager, M. Persson, and P. Meaney, "Application of two-dimensional discrete dipole approximation in simulating electric field of a microwave breast imaging system.," *IEEE Journal of Electromagnetics, RF and Microwaves in Medicine and Biology, Electromagnetics, RF and Microwaves in Medicine and Biology, IEEE Journal of, IEEE J. Electromagn. RF Microw. Med. Biol*, vol. 3, no. 2, pp. 80 – 87, 2019.

[18] M. Slaney, A. Kak, and L. Larsen, "Limitations of imaging with first-order diffraction tomography.," *IEEE Transactions on Microwave Theory and Techniques, Microwave Theory and Techniques, IEEE Transactions on, IEEE Trans. Microwave Theory Techn*, vol. 32, no. 8, pp. 860 – 874, 1984.

[19] C. Nordling and J. Österman, *Physics Handbook*. Studentlitteratur, 2006.

[20] M. Lazebnik, C. Watkins, J. Booske, S. Hagness, L. McCartney, D. Popovic, M. Okoniewski, M. Lindstrom, J. Harter, S. Sewall, and A. Magliocco, "A large-scale study of the ultrawideband microwave dielectric properties of normal breast tissue obtained from reduction surgeries.," *Physics in Medicine and Biology*, vol. 52, no. 10, 2007.

[21] K. Yee, "Numerical solution of initial boundary value problems involving maxwell's equations in isotropic media," *IEEE Transactions on Antennas and Propagation*, vol. 14, no. 3, pp. 302–307, 1966.

[22] Synopsys, "Finite-Difference Time-Domain Method." `https://www.synopsys.com/glossary/what-is-fdtd.html`, 2023. Accessed on May 19, 2023.

[23] A. Fhager, M. Gustafsson, and S. Nordebo, "Image Reconstruction in Microwave Tomography Using a Dielectric Debye Model.," *IEEE Transactions on Biomedical Engineering, Biomedical Engineering, IEEE Transactions on, IEEE Trans. Biomed. Eng*, vol. 59, no. 1, pp. 156 – 166, 2012.

[24] A. Fhager, *Microwave tomography.* Doktorsavhandlingar vid Chalmers tekniska högskola: Ny serie 2468, Chalmers tekniska högskola, 2006.

[25] D. R. Lynch, *Numerical Partial Differential Equations for Environmental Scientists and Engineers*. Springer New York, NY, 2004.

[26] K. Paulsen, P. Meaney, M. Moskowitz, and J. Sullivan, J.M., "A dual mesh scheme for finite element based reconstruction algorithms.," *IEEE Transactions on Medical Imaging, Medical Imaging, IEEE Transactions on, IEEE Trans. Med. Imaging*, vol. 14, no. 3, pp. 504 – 514, 1995.

[27] P. Meaney, N. Yagnamurthy, and K. Paulsen, "Pre-scaled two-parameter gauss-newton image reconstruction to reduce property recovery imbalance.," *Physics in Medicine and Biology*, vol. 47, no. 7, pp. 1101–1119 – 1119, 2002.

[28] . . Meaney, P.M. (1, S. . . . Geimer, and K. . . . Paulsen, "Two-step inversion with a logarithmic transformation for microwave breast imaging:.," *Medical Physics*, vol. 44, no. 8, pp. 4239–4251 – 4251, 2017.

[29] M. J. Burfeindt, T. J. Colgan, R. O. Mays, J. D. Shea, N. Behdad, B. D. Van Veen, and S. C. Hagness, "MRI-derived 3D-printed breast phantom for microwave breast imaging validation," *IEEE Antennas and Wireless Propagation Letters*, vol. 11, pp. 1610–1613, 2012.

DEPARTMENT OF ELECTRICAL ENGINEERING
CHALMERS UNIVERSITY OF TECHNOLOGY
Gothenburg, Sweden
www.chalmers.se

CHALMERS
UNIVERSITY OF TECHNOLOGY